Master Thesis

액츄에이터 오류가 있는 병렬 로봇 시스템을 위한 내고장 제어기법 연구

Fault-tolerant control scheme for a parallel robotic system with actuator fault

The Graduate School
of University of Ulsan
Department of Mechanical Engineering

Le Duc Vinh

Fault-tolerant control scheme for a parallel robotic system with actuator fault

Supervisor: Ha Cheolkeun

A Dissertation

Submitted to
The Graduate School of University of Ulsan
In partial fulfillment of the Requirements
For the Degree of

Master of Science

by

Le Duc Vinh

Department of Mechanical Engineering
Ulsan, Korea
August 2022

Fault-tolerant control scheme for a parallel robotic system

with actuator fault

This certifies that the thesis of Le Duc Vinh is approved by

Committee Chairman:	Prof. Shin Ji-chul
Committee member:	Dr. Choi Hyung Sik
Committee member:	Prof. Ha Cheolkeun

Department of Mechanical Engineering

Ulsan, Korea

August 2022

Fault-tolerant control scheme for a parallel robotic system

with actuator fault

This certifies that the thesis of Le Duc Vinh is approved by

Committee Chairman: 신 지 철

Committee member: 최 형 식

Committee member: 하 철 근

Department of Mechanical Engineering

Ulsan, Korea

August 2022

ACKNOWLEDGMENT

First of all, I am very grateful to Professor Cheolkeun Ha for his sincere advice, invaluable knowledge, and encouragement to complete my master's program at University of Ulsan.

I am fortunate that I have a lovely family, with their endless support, I overcame difficulties to complete this 2-year journey.

I would like to thank my girlfriend Nguyen Thi Phuong for her mental care and for encouraging me throughout this journey

I would like to thank my friends Le Quang Dan and Tran Quang Huy for their care and support from the early days and throughout later studies.

I would also like to thank all my friends who have accompanied and shared with me the past journey.

I also take this opportunity to express a deep sense of gratitude to all employees and professors at Mechanical Engineering Department for their wonderful work.

ABSTRACT

Thanks to the rapid development of technology science and computer, robotic systems are widely used and play an increasingly important role in human life these days. They are used to perform complicated tasks in many fields such as industrial manufacturing, medicine, civil engineering, and aerospace. Nevertheless, in practice, there are some inevitable problems during the operation of robots, such as uncertainties, disturbances, and unmodeled dynamics and friction which may lead to a significant destabilization of the system. Furthermore, the occurrence of faults in systems seriously reduces the safety and reliability of robotic systems. This has caused great obstacles and challenges in designing controllers for robot manipulators. Therefore, the requirement for precise and robust control under the existence of uncertainties, disturbances and faults has attracted a massive number of researchers over the past decades. In this thesis, a fault-tolerant control (FTC) is proposed for a parallel robotic system. To obtain the robustness and a fast finite-time convergence, a nonsingular fast terminal sliding mode control (NFTSMC) is used. In addition, an extended state observer (ESO) is applied for the control scheme to estimate uncertainties, disturbances, and faults. To increase the convergence speed and alleviate the chattering phenomenon, a novel reaching law is proposed which gives the system a quick reaching speed. Finally, a novel FTC that ensures robustness to disturbances and faults is developed based on the NFTSMC, the ESO, and the proposed reaching law. Consequently, the proposed FTC has outstanding features such as high tracking performance, a decrease in the effects of disturbances and faults, a fast convergence speed in finite time, and less chattering. The simulation and experiment results demonstrate the efficiency of the proposed FTC compared to other control schemes. Besides. in the real life, the application of the Stewart Platform is very diverse and this research will investigate one of its applications, a haptic device. The haptic device based on the Stewart Platform is developed by a combination of an admittance model and the proposed FTC. The admittance model transforms a force to the desired trajectory while the proposed FTC is used to track the reference trajectory resulting from the admittance model. Accordingly, the haptic device is applied for teleoperation of a mobile robot with force feedback that helps the operator prevent the robot from colliding obstacles and improve the task performance. The experimental results will demonstrate the effectiveness of the proposed haptic device.

Keywords: Fault-tolerant control, sliding mode control, Reaching law, Extended state observer, Parallel robot, Stewart platform, haptic device, admittance control, teleoperation.

TABLE OF CONTENTS

ACKNOWLEDGMENT 1
ABSTRACT 2
TABLE OF CONTENTS 4
LIST OF FIGURES 6
LIST OF TABLES 8
1. INTRODUCTION 9
1.1 Overview 9
1.2 Research objectives 13
1.3 Outline 14
2. DESIGN AND ANALYSIS OF CONTROL SCHEME 15
2.1 Kinematic of Stewart Platform 15
2.2 Dynamics of the Stewart Platform 17
2.3 Extended state observers for estimation of the uncertainty, disturbance, and fault 18
2.4 A new reaching law 19
2.4.1 Description 19
2.4.2 Convergence analysis 22
2.5 Design of a fault-tolerant control 24
3. EVALUATION OF SIMULATION AND EXPERIMENT RESULTS 27
3.1 Simulation results 27
3.2 Experiment results 37
4. FAULT TOLERANT CONTROL FOR HAPTIC DEVICE IN TELEOPERATION 49
4.1 Introduction 49
4.2 Admittance model 50
4.3 Experiment 51
4.3.1 The performance of the proposed FTC for the haptic device 51
4.3.2 Teleoperation of a mobile robot in the virtual environment 54

5. CONCLUSION **57**
6. LIMITATIONS AND FUTURE WORKS **59**
PUBLICATIONS **60**
REFERENCE **61**

LIST OF FIGURES

Figure 1. a) The Stewart Platform.; b) Top view. 9
Figure 2. The application of Stewart platform in a). Flight Simulator, b) Haptic device. 10
Figure 3. Schematic diagram of a Stewart platform 16
Figure 4. The value of function sign(s) and tanh(s) 21
Figure 5. The value of s. a) s(0) = 10; b) s(0) = 1 22
Figure 6. Block diagram of the control scheme 26
Figure 7. Stewart Platform in MATLAB/SIMULINK 27
Figure 8. The tracking trajectory and performance of NFTSMC, FTC-NFTSMC1, and Proposed FTC for the SP in the simulation 31
Figure 9. Input Force at each leg of the SP for NFTSMC, FTC-NFTSMC1, and Proposed FTC in the simulation 32
Figure 10. The tracking trajectory and performance of FTC-NFTSMC2-QPRL, FTC-NFTSMC2-DPRL, and Proposed FTC for the SP in the simulation 36
Figure 11. Input Force at each leg of the SP for FTC-NFTSMC2-QPRL, FTC-NFTSMC2-DPRL, and Proposed FTC in the simulation 37
Figure 12. Actual Stewart Platform 38
Figure 13. Scheme of the system 38
Figure 14. The tracking trajectory and performance of NFTSMC, FTC-NFTSMC1, and Proposed FTC for the actual SP in the experiment 42
Figure 15. Input force at each leg of the actual SP for NFTSMC, FTC-NFTSMC1, and Proposed FTC in the experiment 43
Figure 16. The tracking trajectory and performance of FTC-NFTSMC2-QPRL, FTC-NFTSMC2-DPRL, and Proposed FTC for the actual SP in the experiment 47
Figure 17. Input Force at each leg of the actual SP for FTC-NFTSMC2-QPRL, FTC-NFTSMC2-DPRL, and Proposed FTC in the experiment 48
Figure 18. Haptic device based on Stewart Platform 51
Figure 19. Human-haptic device cooperation scheme 52
Figure 20. The performance of the haptic device using NTSMC, FTC-NFTSMC1, and Proposed FTC 53
Figure 21. Human-haptic device for teleoperation of a mobile robot 54
Figure 22. A mobile robot in a virtual environment 55

Figure 23. Mapping a logical point (x, y) to motion parameters (speed rate, turning rate) 55
Figure 24. Experimental results of teleoperation. a) Movement of the haptic handle to control a mobile robot. b) Contact force on the haptic handle 56

LIST OF TABLES

Table 1. Parameters of three controllers NFTSMC, FTC-NFTSMC1, and Proposed FTC in the simulation 29
Table 2. The mean absolute error comparison of NFTSMC, FTC-NFTSMC1, and Proposed FTC in the simulation 30
Table 3. Parameters of three controllers FTC-NFTSMC2-QPRL, FTC-NFTSMC2-DPRL, and Proposed in the simulation 33
Table 4. The mean absolute error of FTC-NFTSMC2-QPRL, FTC-NFTSMC2-DPRL, and Proposed in the simulation 34
Table 5. Parameters of three controllers NFTSMC, FTC-NFTSMC1, and Proposed FTC in the experiment 39
Table 6. The mean absolute error comparison of NFTSMC, FTC-NFTSMC1, and Proposed FTC in the experiment 40
Table 7. Parameters of three controllers FTC-NFTSMC2-QPRL, FTC-NFTSMC2-DPRL, and Proposed FTC in the experiment 44
Table 8. The mean absolute error comparison of FTC-NFTSMC2-QPRL, FTC-NFTSMC2-DPRL, and Proposed FTC in the experiment 45
Table 9. The mean absolute errors of the haptic device for x and y directions 53

1. INTRODUCTION

1.1 Overview

A parallel manipulator is a mechanical system that comprises a moving base connected to a fixed base by several computer-controlled parallel chains called legs. The well-known parallel robot is formed from six linear actuators that support the movable platform. This architecture is called Stewart Platform (SP), which is first developed and used by Gough and Stewart. Figure 1 shows a typical Stewart Platform.

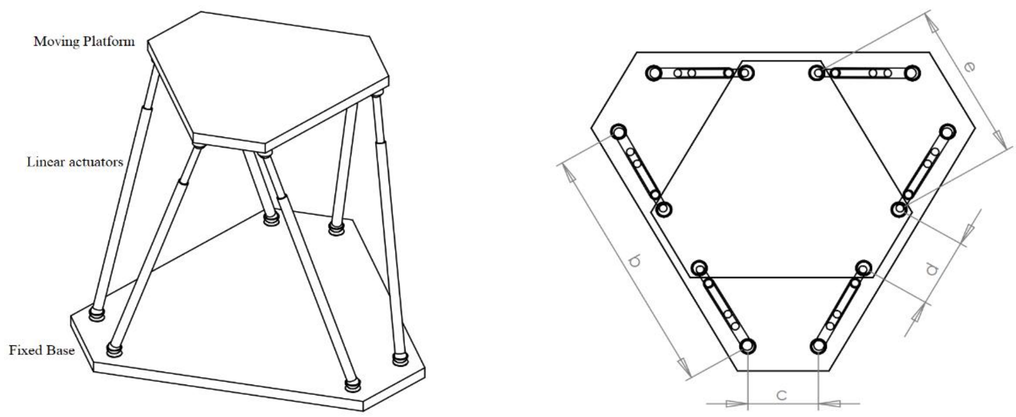

Figure 1. a) The Stewart Platform.; b) Top view.

The desired position and orientation of the moving platform can be obtained by changing the lengths of the legs. The parallel robot has outstanding advantages such as high precision, good rigidity, and higher payloads compared with other serial robots. Hence, it is extensively applied in industry, telescopes, haptic devices, flight and vehicle simulators, entertainment, and medical instruments [1]–[3]. We can see the application of Stewart Platform in Flight simulators and haptic devices in Figure 2.

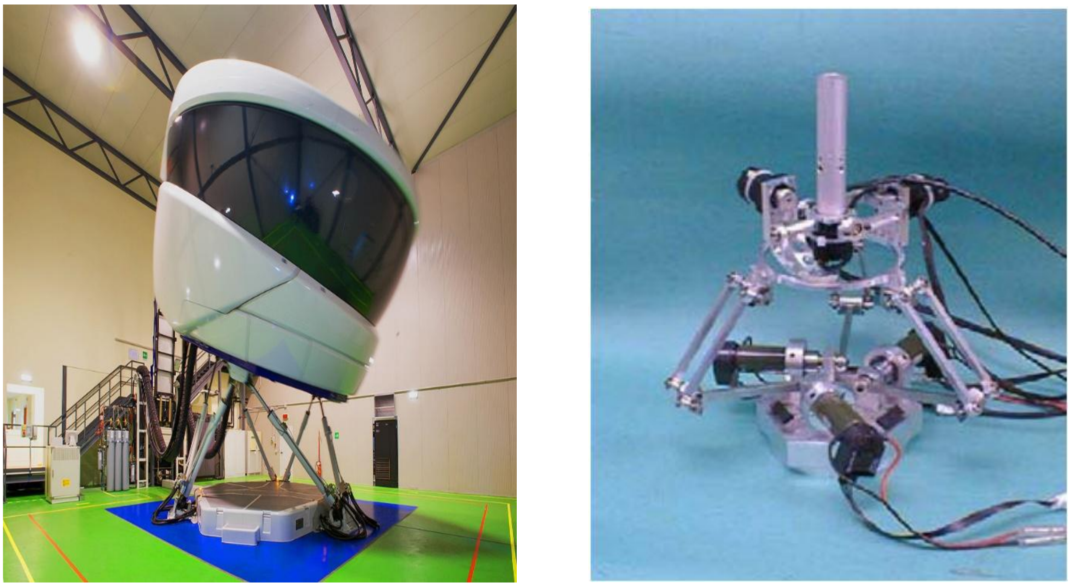

a) b)

Figure 2. The application of Stewart platform in a). Flight Simulator, b) Haptic device.

Nonetheless, due to the inherent complexity in the kinetic analysis of its closed-loop structure, the application of the SP is often challenging. Hence, various kinematic and dynamic investigations have been reported in the literature [4]–[12], and several control technologies for the SP have been studied over the years such as adaptive control [13], neural network control [14], and sliding mode control (SMC) [15]. Among them, SMC possesses fascinating characteristics of robustness to disturbances and uncertainties, and low sensitivity to noise. Nevertheless, conventional SMC cannot ensure that the states of the system approach the equilibrium point in finite time.

Therefore, to ensure that the system state quickly converges in finite time, Nonsingular Fast Terminal Sliding mode control (NFTSMC) was developed and has received much attention from many researchers [16], [17]. It not only preserves the robustness of the traditional SMC, but also has fast convergence in finite time and avoids the singularity issue of Fast Terminal Sliding mode control (FTSMC). Thus, the SP using the conventional controllers or NFTSMC can operate well in normal operation. However, in practice, there might be faults occurring in the system and the conventional controllers or NFTSMC alone cannot ensure the stability of the system. Therefore, there have been many investigations of this problem over the years, and some fault-tolerant technologies have been proposed to increase the safety and reliability of robotic systems when faults occur. The fault-tolerant control can maintain the acceptable performance of the system during the system operation under the occurrence of faults until the system is checked and fixed.

In general, there are two major types of Fault-tolerant control (FTC): passive FTC (PFTC) [18], [19] and active FTC (AFTC) [20], [21]. A PFTC is designed without a fault diagnosis module for normal and fault operation, and depends on the robust capability of the controllers to address lumped disturbances, uncertainty, and faults. The most notable feature of PFTC is its quick response to the occurrence of faults because it does not take time to wait for the fault feedback; however, its ability to compensate for high-magnitude faults is restricted. As a result, there are some limitations in the application of PFTC in actual systems.

In contrast, the key feature of AFTC is its use of an estimation module to compensate for the unpredictable faults in mechanical components, sensors, and actuators to preserve the stability of the system within performance requirements. The robust response of AFTC to faults primarily depends on the efficiency of the estimation module. Hence, a series of active fault-tolerant strategies have been developed for robotic systems based on various observers, such as the sliding mode observer [22], the fuzzy observer [20], and the extended state observer (ESO) [21]. Compared to the other methods, the ESO is an efficient way to estimate faults and is easy to implement in practice. Nevertheless, it is well known that the conventional ESO has several drawbacks, such as the peaking phenomenon that can cause serious stability deterioration of the overall system [23], and its trade-off between the speed of estimation and insensitivity to measurement noise [24]. Many researchers have introduced solutions to decreasing the magnitude of peaking and ensuring the robustness to measurement noise [25]–[27]. In [27], Ran et al. proposed a new ESO that was effective in lessening the peaking issue and had improved sensitivity to measurement noise. Thus, given the significant benefits mentioned above, in this study, a NFTSMC and an ESO [27] are applied in a FTC scheme to considerably improve its performance regardless of the presence of faults in the SP.

Although the accuracy of the system can be improved by the FTC schemes described above, researchers have developed various methods to speed up the reaching rate and diminish chattering which is a major issue in SMC. The chattering problem not only destabilizes the system but also seriously affects its practical applications. Hence, it is of great interest to resolve this issue, and strategies such as the boundary layer method [28], [29], high-order SMC [30], [31], and the reaching law SMC method [32]–[36] have been developed. Of these, the reaching law SMC has attractive advantages due to not only its ability to effectively decrease the chattering issue, but also to improve the approaching phase rate.

In [32], three continuous-time reaching laws were proposed by Gao et al. First, the constant rate reaching law is a simple method that makes the state slide on the sliding surface at a constant rate. Its drawback is the trade-off between the speed of the approaching phase and the magnitude of oscillation in the sliding phase. Next, a modification to the constant reaching law, called the constant plus proportional rate reaching law, can reduce the oscillation to a certain level. The final method is the power rate reaching law, which can decrease chattering.

Based on these methods, several other deep investigations on reaching law have been produced over the years. Wang [33] used a double-power reaching law to further enhance the efficiency of the power reaching law and decline the chattering issue, and an improved double-power reaching law was proposed by Tao [34]. Fallaha [35] introduced the exponential reaching law, which can increase the convergence speed and reduce oscillation. Yang [36] designed a piecewise fast multi-power reaching law based on the fast-power and double-power reaching laws. Generally, the power reaching law has excellent reaching performance and less chattering.

Inspired by these aforementioned works, a new reaching law (NRL) is proposed in this paper to further reduce the reaching time and the chattering problem. The finite-time stability of this new reaching law is demonstrated, as well as its ability to give the system a fast reaching speed. The dynamic coefficient is used to accelerate the convergence rate and minimize the chattering amplitude when the system approaches the sliding surface. As a result, this thesis will illustrate the performance of the proposed FTC scheme by combining NFTMSC, ESO [27], and the NRL, which has the benefits of easy implementation, singularity avoidance, robustness in uncertainties and faults, a decrease in the peaking issue, high accuracy, chattering alleviation, and rapid convergence in finite time.

1.2 Research objectives

The main objective of this thesis is to introduce a new fault-tolerant control for a typical parallel robot called Stewart Platform and the application of the Stewart Platform as a haptic interface for teleoperation. First, NFTSMC possesses fascinating characteristics of robustness to disturbances and uncertainties, low sensitivity to noise, singularity problem rejection, and a fast convergence in finite time. Therefore, NFTSMC is used in the fault-tolerant control scheme to ensure the stability of the system under the existence of uncertainties and disturbances.

However, the chattering phenomenon is a major problem in SMC. It is necessary to develop solutions to this problem. Various methods mentioned above were proposed over the past years such as boundary layer method, high-order SMC, and the reaching law SMC method. This dissertation proposed an improved reaching law which gives the system a chattering alleviation and enhancement in convergence speed of the system.

In addition, to increase the reliability and safety of the system in the presence of faults, an ESO needs to be applied for the control scheme to compensate for the unpredictable faults. The stability of the proposed FTC for the system is proven by Lyapunov theory.

Next, this thesis will illustrate the effectiveness of the proposed fault-tolerant control for a Stewart Platform. In the simulation and experiment parts, a comparison between the proposed FTC and the control scheme without the estimation module is shown to demonstrate the usefulness of the ESO [27] in the proposed FTC under the occurrence of faults. Besides, this study compares the performance of the proposed FTC with the control schemes using the other reaching laws to prove the effect of the NRL on enhancing the reaching speed. Accordingly, the validity of the proposed FTC using the new ESO [27] and the proposed reaching law is evaluated

Finally, a haptic device based on the Stewart platform is constructed by using the admittance model and the proposed FTC. The fault-tolerant control for the haptic device for teleoperation of a mobile robot is investigated.

1.3 Outline

The remainder of the thesis is organized as follows: Section 2 presents the kinematic and dynamic of Stewart Platform and Extended state observer, the new reaching law, and the design procedure of the proposed fault-tolerant control for Stewart Platform; The results of the control performance in the simulation and experiment are given in Sections 3. Section 4 introduces the fault-tolerant control for a haptic device in teleoperation. Finally, the conclusions and the limitation and future works are discussed in Section 5 and Section 6, respectively.

2. DESIGN AND ANALYSIS OF CONTROL SCHEME

In this section, the dynamic model of Stewart Platform is presented in section 2.1, followed by the extended state observer used to estimate the uncertainties, disturbances, and faults of the system in section 2.2. The description and the convergence analysis of the new reaching law are described in section 2.3, and eventually, section 2.4 shows the design procedure of the proposed fault-tolerant control for Stewart Platform.

2.1 Kinematic of Stewart Platform

There are two types of kinematic analysis, known as inverse and forward kinematics, very important and useful in the design and control of SP. The inverse kinematics calculates the leg lengths corresponding to a given end-effector position. Its solution is straightforward and unique. The forward kinematics transform leg coordinates into the reference coordinates of the end-effector, i.e. given the lengths of six variable legs, L, find the transformation of coordinates representing the position and orientation of the top plate, X, with respect to inertia reference frame XYZ. The forward kinematics (FK) problem requires the solution of a series of non-linear equations and usually has multiple solutions. The most general solution requires the formulation of a 16th or higher-order polynomial equation [6], [7], [10], which in turn has to be solved by some numerical methods. Geng et al. used neural networks to find the forward kinematics solution of Stewart platform [8]. Chifu Yang et al. implemented Newton-Raphson method for forward kinematic analysis [9]. By contrast to inverse kinematics, forward kinematics is neither well behaved nor easily described.

A SP is mainly constructed of six prismatic joints, a fixed base, and a moving platform shown in Figure 3. We assume that the position of the center of the moving platform is $P(p_x, p_y, p_z)$ with respect to a coordinate {O} placed at the center of the fixed base, and the orientation of the moving platform is described by a rotation of angle φ_x about the fixed x-axis of {O} (roll), then about the fixed y-axis of {O} by angle φ_y (pitch) and about the fixed z-axis of {O} by angle φ_z (yaw). Thus, the rotation matrix can be written as

$$ {}^{O}_{P}R_{XYZ}(\varphi_x,\varphi_y,\varphi_z)=\begin{bmatrix} c\varphi_z\,c\varphi_y & c\varphi_z\,s\varphi_y\,s\varphi_x - s\varphi_z\,c\varphi_x & c\varphi_z\,s\varphi_y\,c\varphi_x + s\varphi_z\,s\varphi_x \\ s\varphi_z\,c\varphi_y & s\varphi_z\,s\varphi_y\,s\varphi_x + c\varphi_z\,c\varphi_x & s\varphi_z\,s\varphi_y\,c\varphi_x - c\varphi_z\,s\varphi_x \\ -s\varphi_y & c\varphi_y\,s\varphi_x & c\varphi_y\,c\varphi_x \end{bmatrix} \tag{1}$$

where s denotes sine and c denotes cosine

The position of the center of the moving platform with respect to {O} is $P=[\,p_x, p_y, p_z]^T$

According to Figure 3, we have:

$$a_i + A_iB_i = p + {}^{O}_{P}Rb_i \tag{2}$$

Where a_i denotes the position vector of the *i*th universal joint in the fixed base with respect to {O}. b_i denotes the position vector of the *i*th ball joint in the moving platform with respect to {P}. p is the position vector of the center point P of the moving platform.

The leg length of Stewart Platform

$$d_i = \left\| p + {}^{O}_{P}Rb_i - a_i \right\| = \sqrt{d_{ix}^2 + d_{iy}^2 + d_{iz}^2} \tag{3}$$

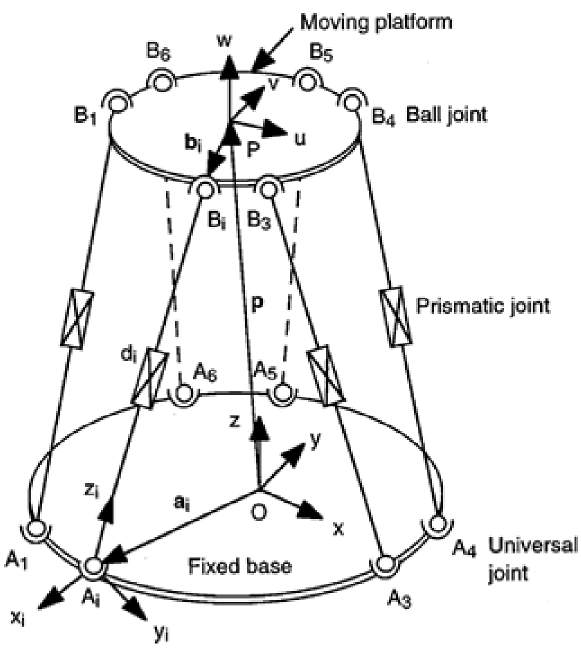

Figure 3. Schematic diagram of a Stewart platform

2.2 Dynamics of the Stewart Platform

The dynamics of the SP were studied in much previous research [11], [12]. Generally, the dynamic equation of the SP can be given as follows:

$$F = J^T\tau = M(X)\ddot{X} + V(X,\dot{X}) + \mathrm{G}(X) + f_d \tag{4}$$

where $\tau \in R^n$ is the vector of the force of the actuator, J is a Jacobian matrix, F is the vector of force in Cartesian space, *M(X)* is an inertia matrix, $V(X,\dot{X})$ is the vector of Coriolis/centrifugal force, G*(X)* is the vector of gravitation force, f_d is the unknown disturbance of the system, and $X = [p_x, p_y, p_z, \varphi_x, \varphi_y, \varphi_z]^T$.

The parameters of the system dynamics can be expressed as nominal and deviational as follows: $M = M_o + \Delta M,\ V = V_o + \Delta V,\ G = \mathrm{G}_o + \Delta G$ where M_o, V_o, and G_o are the nominal model dynamics and $\Delta M, \Delta V, \Delta G$ are unknown model uncertainties. (4) can be rewritten as:

$$F = J^T\tau = M_o\ddot{X} + V_o + \mathrm{G}_o + \Psi \tag{5}$$

where $\Psi = \Delta M.\ddot{X} + \Delta V + \Delta G + f_d$

However, in practice, there are certain faults, such as sensor faults, mechanical faults, and actuator faults. In this paper, we consider actuator faults.

According to Li and Tong [37], actuator faults can be divided into bias fault and gain fault. The actuator fault model can be written as:

$$\tau_i^f = (1-\rho_i(t))\tau_i + f_i(t) \quad (t > t_f),\ \ i = 1,2,...,n \tag{6}$$

where $f_i(t)$ denotes a bounded signal (bounded function) and $\rho_i(t)$ is the unknown remaining control rate, $0 \le \rho_i(t) \le 1$. τ_i is the force of the *i*th actuator without fault. τ_i^f denotes the force of the *i*th actuator when the fault occurs and t_f is the time of occurrence of the fault.

In general, the input vector of the SP can be written as:

$$\tau^f = (I - \rho(t))\tau + f(t) \tag{7}$$

where $\tau^f = \left[\tau_1^f, \tau_2^f, ..., \tau_6^f\right]^T$, $\tau = \left[\tau_1, \tau_2, ..., \tau_6\right]^T$, $\rho = diag\{\rho_1, \rho_2, ..., \rho_6\}$, $f = \left[f_1, f_2, ..., f_6\right]^T$, and I is an identity matrix 6×6.

Substituting (7) into (5) yields:

$$\ddot{X} = M_o^{-1}\zeta - M_o^{-1}\left(J^T \rho(t)\tau - J^T f(t) + \Psi\right) \tag{8}$$

where $\zeta = F - V_o - G_o$

2.3 Extended state observers for estimation of the uncertainty, disturbance, and fault

The dynamic model (8) can be rewritten in the state space as follows:

$$\begin{cases} \dot{x}_1 = x_2 \\ \dot{x}_2 = M_o^{-1}\zeta - M_o^{-1}\left(J^T \rho(t)\tau - J^T f(t) + \Psi\right) \end{cases} \tag{9}$$

where $x_1 = X \in R^n, x_2 = \dot{X} \in R^n$.

We define $x_3 = -M_o^{-1}\left(J^T \rho(t)\tau - J^T f(t) + \Psi\right)$ to be the extended state of the system (9), then (9) becomes:

$$\begin{cases} \dot{x}_1 = x_2 \\ \dot{x}_2 = M_0^{-1}\zeta + x_3 \end{cases} \tag{10}$$

According to [38], a conventional linear ESO can be designed as:

$$\begin{cases} \dot{\hat{x}}_1 = \hat{x}_2 + \dfrac{\alpha_1}{\mu}\left(x_1 - \hat{x}_1\right) \\ \dot{\hat{x}}_2 = M_o^{-1}\zeta + \dfrac{\alpha_2}{\mu^2}\left(x_1 - \hat{x}_1\right) + \hat{x}_3 \\ \dot{\hat{x}}_3 = \dfrac{\alpha_3}{\mu^3}\left(x_1 - \hat{x}_1\right) \end{cases} \tag{11}$$

where $\hat{x}_1, \hat{x}_2, \hat{x}_3$ are observer states, $\alpha_1, \alpha_2, \alpha_3$ are positive constants chosen so that the polynomial $s^3 + \alpha_1 s^2 + \alpha_2 s + \alpha_3$ is a Hurwitz polynomial, and μ < 1 is a small positive constant.

As aforementioned, some disadvantages of the conventional ESO (11) (ESO1) are the peaking issue and high sensitivity to measurement noise. Hence, a different ESO is proposed by Ran et al. [27] to decrease the influence of these downsides on the system, and it can be described as:

$$\begin{cases} \dot{\phi}_1 = \dfrac{\alpha_1}{\mu}\left(x_1 - \phi_1\right),\ \hat{x}_2 = \dfrac{\alpha_1}{\mu}\left(x_1 - \phi_1\right) \\ \dot{\phi}_2 = M_o^{-1}\zeta + \dfrac{\alpha_2}{\mu}\left(\hat{x}_2 - \phi_2\right), \hat{x}_3 = \dfrac{\alpha_2}{\mu}\left(\hat{x}_2 - \phi_2\right) \end{cases} \tag{12}$$

where $\phi_1, \phi_2 \in R^n$, 0< μ <1 is a small positive constant, and α_1, α_2 are positive constants.

Ran et al. [27] demonstrated the convergence of the new ESO (12) (ESO2) such that there exists δ > 0 and T > 0 such that: $\left|x_i(t) - \hat{x}_i(t)\right| \le \delta,\ 2 \le i \le 3, \forall t \ge T$

2.4 A new reaching law

2.4.1 Description

As mentioned above, many valid methods have been investigated to reduce chattering in SMC. Among them, the improvement of the reaching law in SMC can not only eliminate the oscillation but can also approach the sliding surface rapidly. Thus, many reaching laws have been proposed, such as the quick-power reaching law (QPRL) and the double-power reaching law (DPRL), which have excellent reaching performance. The QPRL is derived by a combination of the power rate reaching and the proportional rate term with the constant coefficients and can be designed as:

$$\dot{s} = -k_1 \left|s\right|^{w_1} \operatorname{sgn}(s) - k_2 s \tag{13}$$

Whereas the DPRL has two power terms and can be described as:

$$\dot{s} = -k_1 |s|^{w_1} \operatorname{sgn}(s) - k_2 |s|^{w_2} \operatorname{sgn}(s) \tag{14}$$

where $k_1 > 0$, $k_2 > 0$, $0 < w_1 < 1$, $w_2 > 1$. s is the sliding surface. The first part in the right hand of the DPRL (14) plays the main role when $|s| < 1$ and while the second part plays the main role when $|s| > 1$

It is well known that the reaching speed of the QPRL (13) is slower than that of the DPRL (14) when the states of the system are far away from the sliding surface, i.e., $|s| \geq 1$, but the reaching speed of the QPRL (13) is faster than that of the DPRL (14) when the states approach the sliding surface, i.e., $|s| < 1$. Taking advantage of the benefits of the QPRL and the DPRL, a new reaching law (NRL) is described as:

$$\dot{s} = -k_3 \tanh\left(\frac{s}{\eta}\right) - k_2 |s|^g \operatorname{sgn}(s) \tag{15}$$

where

$$k_3 = \frac{2k_1}{\varepsilon + (1-\varepsilon)\exp(-c(|s|-1))}$$

$$g = \begin{cases} r & if\ |s| \geq 1 \\ 1 & if\ |s| < 1 \end{cases}, \ r > 1, \text{ positive constant}$$

$k_1, k_2, \varepsilon, c, \eta$ are positive constants, and $0 < \varepsilon < 1$.

In the NRL, the first coefficient and the second power terms can be dynamically changed according to the magnitude of s. In particular, the hyperbolic tangent function is used in the NRL instead of the sign function to further reduce the chattering when the system is close to the sliding surface. Figure 4 shows the value of the sign function sign(s) and tangent function tanh(s). It can be seen that the value of tanh(s) smoothly changes, and when s approaches zero, the magnitude of tanh(s) decreases dramatically to make the first term in (15) decline. It is very helpful to reject the oscillation when the system is near the sliding surface.

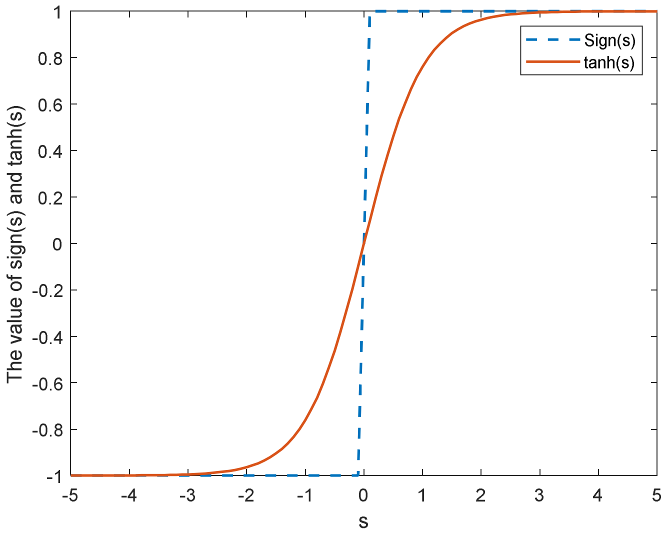

Figure 4. The value of function sign(s) and tanh(s)

For example, the parameters in (13), (14), and (15) are given as $k_1 = 3$, $k_2 = 4$, $w_1 = 0.8$, $w_2 = 1.5$, $r = 1.5$, $\varepsilon = 0.1$, $\eta = 0.1$, $c = 0.2$. We test the convergence speeds of the thee reaching laws for two cases in which the initial value of s is given as s(0) = 10 and s(0) = 1. Figure 5 shows the results of the simulation for the reaching laws. As we can see, when $|s| \geq 1$, the convergence rate of the NRL (15) is faster than that of the DPRL (14). On the other hand, when $|s| < 1$, the convergence speed of (15) is faster than that of the QPRL (13).

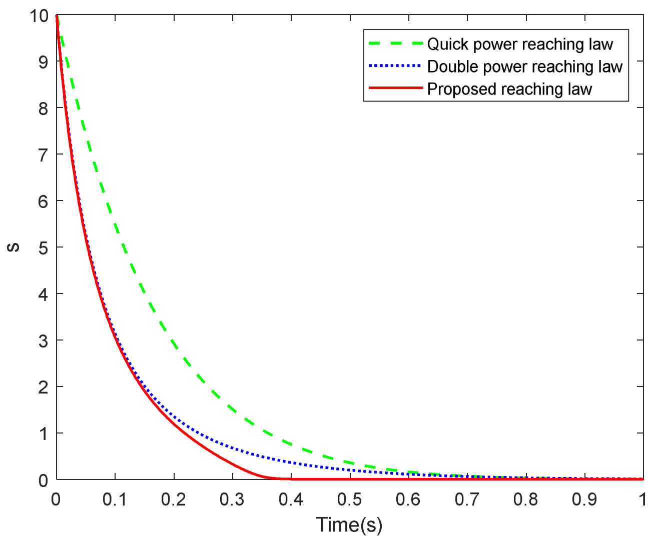

a)

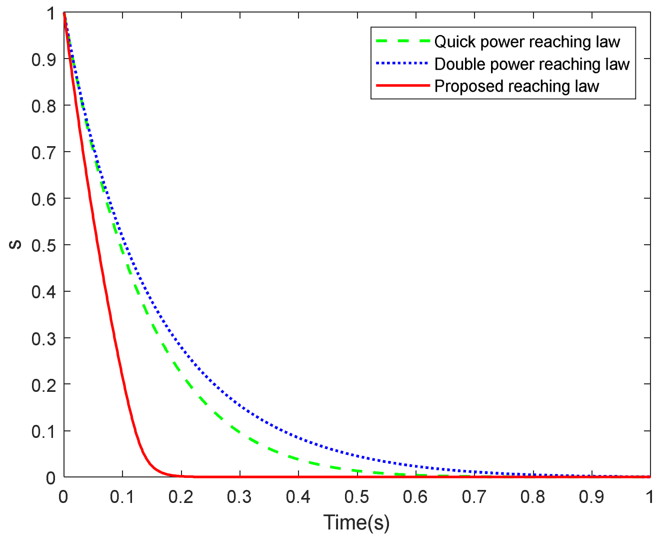

b)

Figure 5. The value of s. a) s(0) = 10; b) s(0) = 1

Remark: From the proposed reaching law (15), k_3 can be dynamically changed according to the value of s. If s increases, k_3 increases that means the reaching rate will be faster. In contrast, when s approaches zero, (15) can be approximately equivalent to the following expression:

$$\dot{s} = -\frac{2k_1}{\varepsilon + (1-\varepsilon)\exp(c)}\tanh\left(\frac{s}{\eta}\right) - k_2 s \quad (16)$$

then $\frac{2k_1}{\varepsilon + (1-\varepsilon)\exp(c)} < \frac{2k_1}{\varepsilon + (1-\varepsilon)\exp\left(-c(|s|-1)\right)}$

which means that k_3 decreases and makes the system obtain the goal of less chattering. Therefore, the NRL can not only have a fast reaching rate in different stages but can also decrease the chattering issue.

2.4.2 Convergence analysis

For the NRL (15), selecting the Lyapunov function $V_1 = 0.5s^2$ and its derivative is:

$$\dot{V}_1 = s\dot{s} = \left(-k_3 s \tanh\left(\frac{s}{\eta} \right) - k_2 \left| s \right|^{g+1} \right) \le 0 \tag{17}$$

Thus, the stability condition can be guaranteed.

Case 1: Assuming s(0) > 1, the reaching process can be divided into two stages: $s(0) \to s = 1$ and $s = 1 \to s = 0$.

For the first stage, $s(0) \to s = 1$, (15) can be written as:

$$\dot{s} = -k_3 \tanh\left(\frac{s}{\eta} \right) - k_2 s^r \tag{18}$$

Hence, the convergence time can be determined as:

$$\int_0^{t_1} dt = \int_1^{s(0)} \frac{1}{k_3 \tanh\left(\frac{s}{\eta} \right) + k_2 s^r} ds < \int_1^{s(0)} \frac{1}{k_2 s^r} ds = \frac{s(0)^{1-r} - 1}{(1-r)k_2} \tag{19}$$

For the second stage, $s = 1 \to s = 0$, (15) can be written as:

$$\dot{s} = -k_3 \tanh\left(\frac{s}{\eta} \right) - k_2 s \tag{20}$$

In practice, s may only approach a value near zero and we assume that the slope of this value is small enough, e.g., 0.001, 0.0001, etc. In this case, there may be a small steady-state error but it probably will not influence the convergence precision of the system. We define the convergence value to be equal to σ approaching zero. Thus, the convergence time can be calculated as:

$$\int_0^{t_2} dt = \int_\sigma^{1} \frac{1}{k_3 \tanh\left(\frac{s}{\eta} \right) + k_2 s} ds < \int_\sigma^{1} \frac{1}{k_2 s} ds = -\frac{\ln(\sigma)}{k_2} \tag{21}$$

Hence, the total time t_1^s can be calculated as:

$$t_1^s = t_1 + t_2 < \frac{1 - s(0)^{1-r}}{(r-1)k_2} - \frac{\ln(\sigma)}{k_2} \tag{22}$$

Case 2: Assuming s(0) < –1, the reaching manner also has two stages: from $s(0) \to s = -1$ and from $s = -1 \to s = 0$. The analysis, in this case, is similar to that of Case 1. Thus, the sum time t_2^s can be calculated as:

$$t_2^s < \frac{1-\left(-s(0)\right)^{1-r}}{(r-1)k_2} - \frac{\ln(\sigma)}{k_2} \tag{23}$$

Overall, the sliding mode s can reach the value approaching 0 in a finite time t^s for any initial condition $s(0)$:

$$t^s < \frac{1-\left|s(0)\right|^{1-r}}{(r-1)k_2} - \frac{\ln(\sigma)}{k_2} \tag{24}$$

2.5 Design of a fault-tolerant control

In this section, a fault-tolerant control based on NFTSMC, ESO2, and the improved reaching law (15) is developed for the SP. The sliding surface of the NFTSMC is defined as:

$$s = e + \lambda_1 e^{l/h} + \lambda_2 \dot{e}^{p/q} \tag{25}$$

where $e = X_d - X$. X_d is the desired trajectory in Cartesian space. X is the practical trajectory in Cartesian space. l, h, p, and q are positive odd integers, $1 < p/q < 2$, $l/h > p/q$, and λ_1 and λ_2 are the positive constants.

Taking the time derivative of (25) yields:

$$\dot{s} = \dot{e} + \lambda_1 \frac{l}{h}\left|e\right|^{\frac{l}{h}-1}\dot{e} + \lambda_2 \frac{p}{q}\left|\dot{e}\right|^{\frac{p}{q}-1}(\ddot{X}_d - \ddot{X}) \tag{26}$$

Substituting (10) into (26) yields:

$$\dot{s} = \dot{e} + \lambda_1 \frac{l}{h}\left|e\right|^{\frac{l}{h}-1}\dot{e} + \lambda_2 \frac{p}{q}\left|\dot{e}\right|^{\frac{p}{q}-1}\left(\ddot{X}_d - M_o^{-1}\zeta - x_3\right) \tag{27}$$

Applying ESO2 and the proposed reaching law (15) for control input, then the proposed FTC law is described as follows:

$$F = F_{eq} + F_s \tag{28}$$

where

$$F_{eq} = M_o\left(\ddot{X}_d + \frac{1}{\lambda_2}\frac{q}{p}\dot{e}^{2-\frac{p}{q}} + \frac{\lambda_1}{\lambda_2}\frac{l}{h}\frac{q}{p}|e|^{\frac{l}{h}-1}\dot{e}^{2-\frac{p}{q}} - \hat{x}_3 + k_2|s|^g \operatorname{sgn}(s)\right) + V_o + G_o \tag{29}$$

is an equivalent control, and

$$F_s = M_o k_3 \tanh\left(\frac{s}{\eta}\right) \tag{30}$$

is a switching term

Theorem:

Considering the SP described in (10) with the nonsingular fast terminal sliding surface defined in (25), the ESO in (12), the proposed reaching law in (15), and the FTC law designed in (28), then the tracking error e will converge to zero within a finite time.

Proof:

Selecting a Lyapunov function as $V_2 = \frac{1}{2}s^2 \geq 0$ and taking the time derivative of V_2, we have:

$$\dot{V}_2 = s\dot{s} = s\left[\dot{e} + \lambda_1\frac{l}{h}|e|^{\frac{l}{h}-1}\dot{e} + \lambda_2\frac{p}{q}|\dot{e}|^{\frac{p}{q}-1}\left(\ddot{X}_d - M_o^{-1}\left(F - V_o - G_o\right) - x_3\right)\right] \tag{31}$$

Substituting (28) into (31), we have:

$$\dot{V}_2 = -\lambda_2\frac{p}{q}k_3 s|\dot{e}|^{\frac{p}{q}-1}\tanh\left(\frac{s}{\eta}\right) - \lambda_2 k_2\frac{p}{q}|\dot{e}|^{\frac{p}{q}-1}|s|^{g+1} + \lambda_2\frac{p}{q}s|\dot{e}|^{\frac{p}{q}-1}(\hat{x}_3 - x_3) \tag{32}$$

$$\dot{V}_2 \leq -\lambda_2\frac{p}{q}k_3 s|\dot{e}|^{\frac{p}{q}-1}\tanh\left(\frac{s}{\eta}\right) - \lambda_2\frac{p}{q}|s||\dot{e}|^{\frac{p}{q}-1}\left(k_2|s|^g - \delta\right) \tag{33}$$

Since $\lambda_2\frac{p}{q}k_3 s|\dot{e}|^{\frac{p}{q}-1}\tanh\left(\frac{s}{\eta}\right) \geq 0$, to ensure that the system is stable, it needs to satisfy the condition as:

$$k_2 |s|^g \geq \delta \tag{34}$$

That means:

$$|s| \geq \left(\frac{\delta}{k_2}\right)^{1/g} \tag{35}$$

When $|s| \leq 1$, it leads to:

$$|s| \geq \frac{\delta}{k_2} \tag{36}$$

This implies that the states of the system can converge in a finite time and δ / k_2 is a convergence region of the sliding mode variable s.

The finite time t_s of (25) is the traveling time from e(tr) to e(tr+ ts) introduced in [16] as:

$$t_s = \frac{\frac{p}{q}|e(0)|^{1-q/p}}{\lambda_1\left(\frac{p}{q}-1\right)} H\left(\frac{q}{p}, \frac{\frac{p}{q}-1}{\left(\frac{l}{h}-1\right)\frac{p}{q}}; 1+\frac{\frac{p}{q}-1}{\left(\frac{l}{h}-1\right)\frac{p}{q}}; -\lambda_1 |e(0)|^{l/h-1}\right) \tag{37}$$

where H(.) denotes Gauss' hypergeometric function.

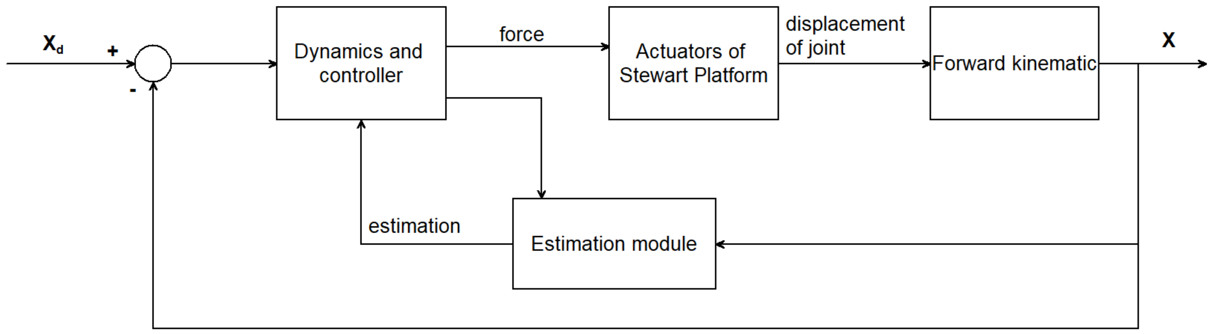

Figure 6. Block diagram of the control scheme

3. EVALUATION OF SIMULATION AND EXPERIMENT RESULTS

3.1 Simulation results

To demonstrate the effectiveness of the proposed FTC, the simulation results are illustrated in this section. First, the mechanical model of the SP was designed in SolidWorks. Next, it was exported to the Simulink environment via the Simscape Multibody link tool, and the simulation was executed in MATLAB/Simulink shown in Figure 7. The parameters of the SP c, b, d, e, mp, I_{xx}, I_{yy}, and I_{zz} were given in SolidWorks as 54 mm, 198 mm, 54 mm, 126 mm, 145 g, 296,223 g.mm^2, 296,223 g.mm^2, and 588,962 g.mm^2, respectively.

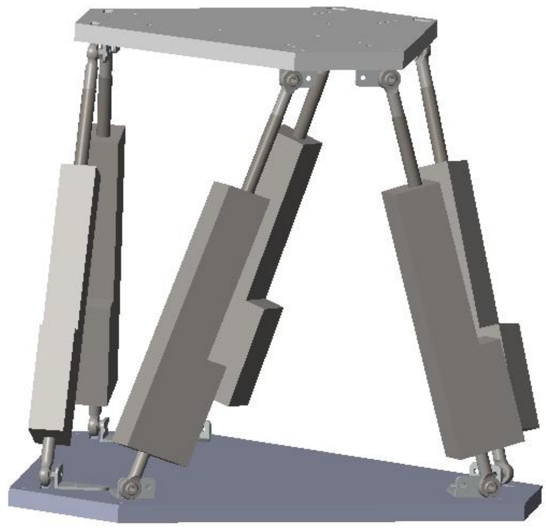

Figure 7. Stewart Platform in MATLAB/SIMULINK

The reference trajectory of the moving platform was described according to the following expression:

$$X_d = \begin{bmatrix} 0.02\sin(0.2\pi t) \ \ (m) \\ 0.02\cos(0.2\pi t) \ \ (m) \\ 0.26 + 0.02\sin(0.2\pi t) \ \ (m) \\ \frac{\pi}{36}\sin(0.2\pi t) \ \ (rad) \\ \frac{\pi}{60}\sin(0.2\pi t) \ \ (rad) \\ \frac{\pi}{45}\sin(0.2\pi t) \ \ (rad) \end{bmatrix} \tag{38}$$

First, the performance of the proposed FTC with the ESO2 (Proposed FTC) was compared to the FTC with the conventional ESO1 (FTC-NFTSMC1) and the NFTSMC without the ESO (NFTSMC). The control input of the NFTSMC can be given as:

$$F = M_o\left(\ddot{X}_d + \frac{1}{\lambda_2}\frac{q}{p}\dot{e}^{2-\frac{p}{q}} + \frac{\lambda_1}{\lambda_2}\frac{l}{h}\frac{q}{p}e^{\frac{l}{h}-1}\dot{e}^{2-\frac{p}{q}} + k_3\tanh\left(\frac{s}{\eta}\right) + k_2|s|^g\,\mathrm{sgn}(s)\right) + V_o + G_o \tag{39}$$

Constants	NFTSMC	FTC-NFTSMC1	Proposed FTC
λ_1	0.1	0.1	0.1
λ_2	0.02	0.02	0.02
l/h	27/19	27/19	27/19
q/p	21/19	21/19	21/19
k_1	5	5	5
k_2	2000	2000	2000
ε	0.1	0.1	0.1
c	0.2	0.2	0.2
η	0.1	0.1	0.1
r	1.1	1.1	1.1
α_1		3	1
α_2		3	1
α_3		1	

μ		0.005	0.005

Table 1. Parameters of three controllers NFTSMC, FTC-NFTSMC1, and Proposed FTC in the simulation

The parameters of three controllers NFTSMC, FTC-NFTSMC1, Proposed FTC, ESO1, and ESO2 were selected in Table 1. The disturbance of the system was assumed as $f_d = 0.01\sin(t)$. It could be assumed that multiple faults arose at the first, third, and fifth actuators at 5 sec. The torque functions with multiple faults were given in (7), where $\rho_1(t) = 0.3 + 0.2\cos(\pi t)$, $\rho_2(t) = 0$, $\rho_3(t) = 0.2 + 0.2\sin(t)$, $\rho_4(t) = 0$, $\rho_5(t) = 0.2 + 0.1\sin(2t)$, $\rho_6(t) = 0$, $f_1(t) = 0.1\sin(t)$, $f_2(t) = 0$, $f_3(t) = 0.5\cos(2t)$, $f_4(t) = 0$, $f_5(t) = \cos(0.5t)$, and $f_6(t) = 0$. In addition, the mean absolute error (MAE) of each controller can be calculated as follows:

$$MAE = \frac{1}{n}\sum_{i=1}^{n}\left|X_{di} - X_i\right| = \frac{1}{n}\sum_{i=1}^{n}\left|e_i\right| \tag{40}$$

where X_{di} is the reference trajectory, X_i is the practical trajectory, n is the sample size $e_i = X_{di} - X_i$.

Figure 8 and Table 2 show the tracking trajectory and performance of NFTSMC, FTC-NFTSMC1, and Proposed FTC. When the faults did not occur in the first five seconds, the tracking performances of controllers were almost the same. However, the performances of the controllers significantly changed after the faults appeared. As shown, the FTC-NFTSMC1 and Proposed FTC had more excellent performance than the NFTSMC because the faults were efficiently estimated and compensated by ESO1 and ESO2. Furthermore, Proposed FTC had less peaking than did FTC-NFTSMC1 and NFTSMC. This exhibited the success in lessening the peaking value of ESO2 in the proposed FTC compared to that of the conventional ESO1.

Controllers	MAE x (m)	MAE y (m)	MAE z (m)	MAE roll (rad)	MAE pitch (rad)	MAE yaw (rad)
NFTSMC	4.726e-05	1.383e-04	4.755e-04	0.0052	0.0035	3.136e-04
FTC-NFTSMC1	4.754e-06	6.274e-05	2.88e-04	4.233e-04	4.119e-04	1.756e-05
Proposed FTC	2.966e-06	5.948e-05	3.179e-04	3.618e-04	3.221e-04	1.374e-05

Table 2. The mean absolute error comparison of NFTSMC, FTC-NFTSMC1, and Proposed FTC in the simulation

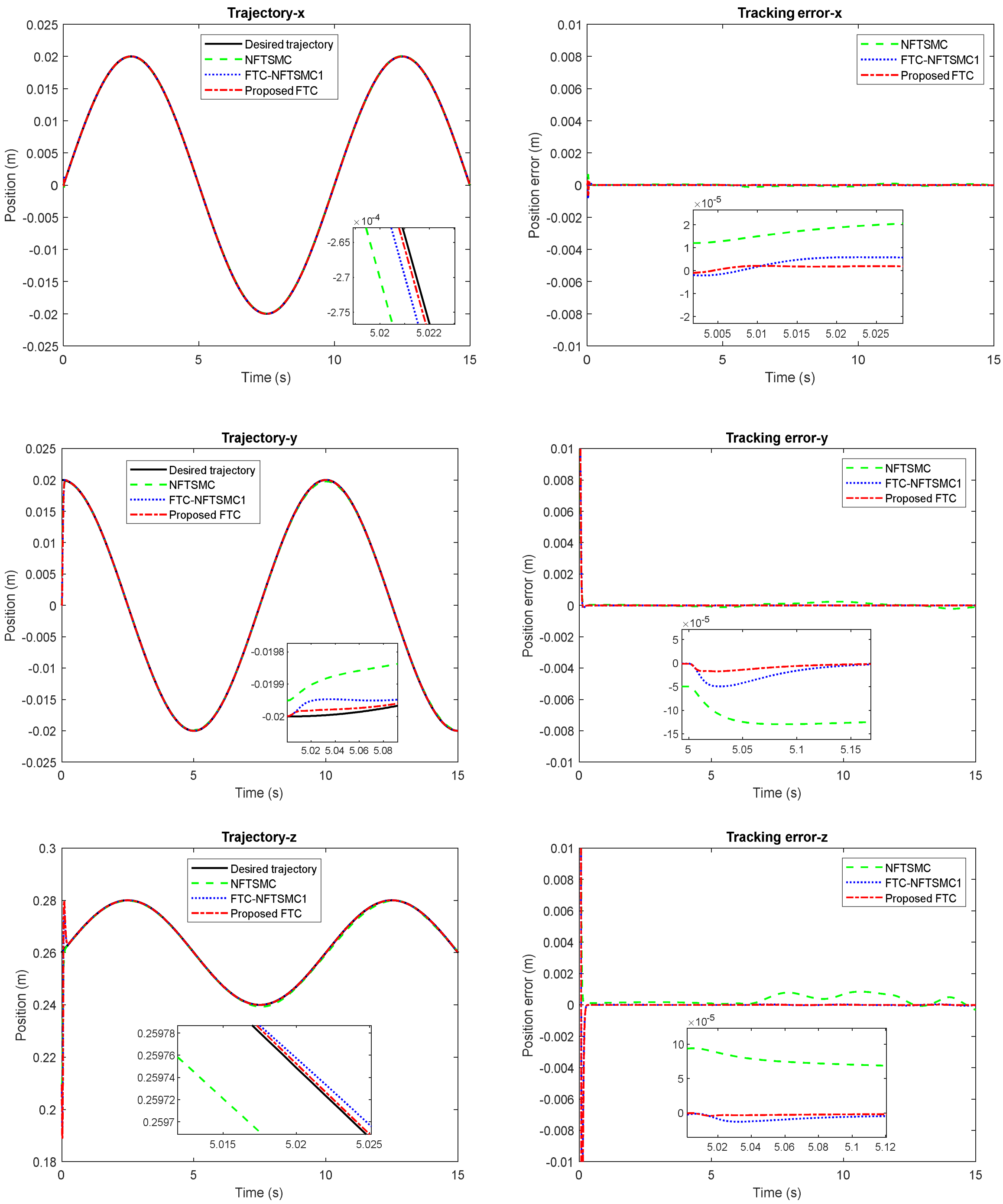

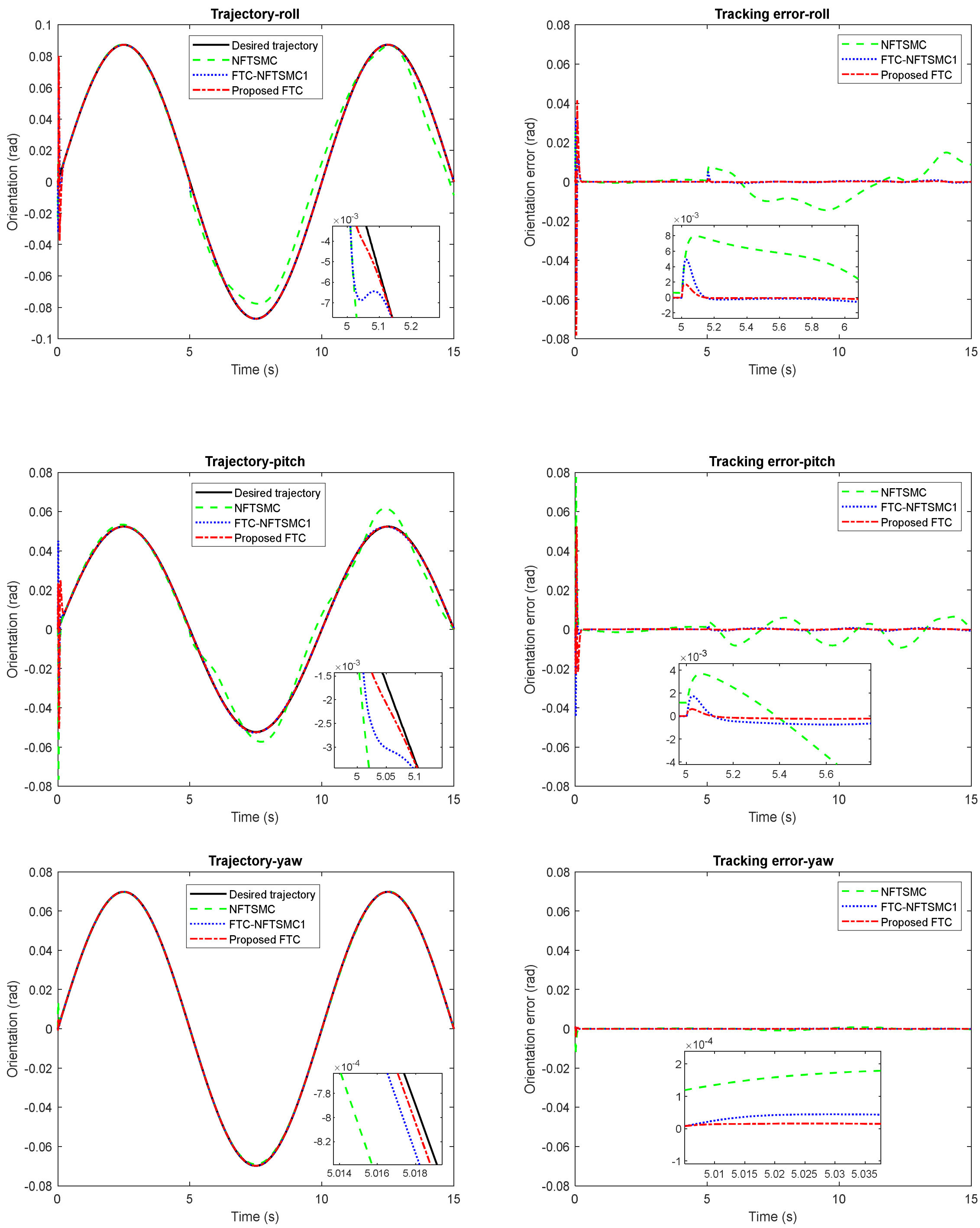

Figure 8. The tracking trajectory and performance of NFTSMC, FTC-NFTSMC1, and Proposed FTC for the SP in the simulation

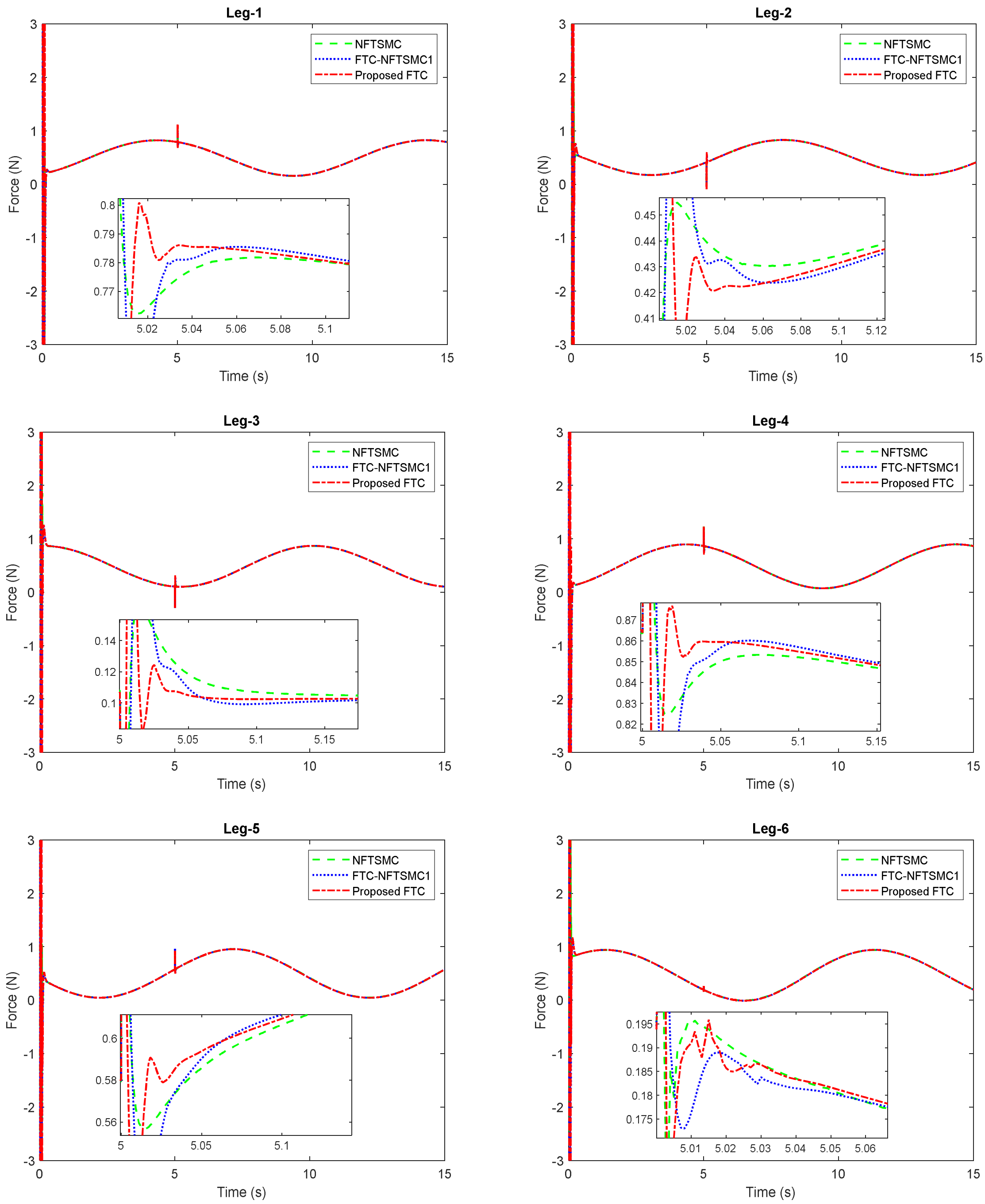

Figure 9. Input Force at each leg of the SP for NFTSMC, FTC-NFTSMC1, and Proposed FTC in the simulation

Next, to verify the effectiveness of the improved reaching law, the performance of the proposed FTC law (28) using the NRL (15) (Proposed FTC) was compared with that of the FTC laws using the QPRL (FTC-NFTSMC2-QPRL) and the DPRL (FTC-NFTSMC2-DPRL) respectively described as:

$$F = M_o\left(\ddot{X}_d + \frac{1}{\lambda_2}\frac{q}{p}\dot{e}^{2-\frac{p}{q}} + \frac{\lambda_1}{\lambda_2}\frac{l}{h}\frac{q}{p}e^{\frac{l}{h}-1}\dot{e}^{2-\frac{p}{q}} - \hat{x}_3 + k_1\left|s\right|^{w_1}\operatorname{sgn}(s) + k_2 s\right) + V_o + G_o \quad (41)$$

$$F = M_o\left(\ddot{X}_d + \frac{1}{\lambda_2}\frac{q}{p}\dot{e}^{2-\frac{p}{q}} + \frac{\lambda_1}{\lambda_2}\frac{l}{h}\frac{q}{p}e^{\frac{l}{h}-1}\dot{e}^{2-\frac{p}{q}} - \hat{x}_3 + k_1\left|s\right|^{w_1}\operatorname{sgn}(s) + k_2\left|s\right|^{w_2}\operatorname{sgn}(s)\right) + V_o + G_o \quad (42)$$

Constants	FTC-NFTSMC2-QPRL	FTC-NFTSMC2-DPRL	Proposed FTC
λ_1	0.1	0.1	0.1
λ_2	0.02	0.02	0.02
l/h	27/19	27/19	27/19
q/p	21/19	21/19	21/19
k_1	5	5	5
k_2	2000	2000	2000
ε	0.1	0.1	0.1
c	0.2	0.2	0.2
η	0.1	0.1	0.1
r			1.1
w_1	0.8	0.8	
w_2		1.1	

Table 3. Parameters of three controllers FTC-NFTSMC2-QPRL, FTC-NFTSMC2-DPRL, and Proposed in the simulation

Proposed FTC, FTC-NFTSMC2-QPRL, and FTC-NFTSMC2-DPRL use the same ESO2. The parameters of the three controllers are given in Table 3. The tracking performances of the three controllers are shown in Figure 10 and Table 4. As we can see, the convergence speed of Proposed FTC was faster than that of FTC-NFTSMC2-QPRL and FTC-NFTSMC2-DPRL. Besides, all three controllers had good tracking errors in the presence of the actuator faults, which demonstrated the efficiency of ESO2 compensating the faults regardless of which reaching law was used in the FTC law. In addition, when the faults occurred, Proposed FTC and FTC-NFTSMC2-QPRL had slightly better performance than FTC-NFTSMC2-DPRL because the convergence speed of FTC-NFTSMC2-DPRL was slightly slower than the other two when the system states changed around the sliding surface, as mentioned in Section II. Therefore, the proposed FTC scheme had not only a fast transient response but also robustness to the lumped uncertainty and faults of the system and the decrease of the peaking value. The control signals of all controllers are illustrated in Figure 9 and Figure 11.

Controllers	MAE x (m)	MAE y (m)	MAE z (m)	MAE roll (rad)	MAE pitch (rad)	MAE yaw (rad)
FTC-NFTSMC2-QPRL	3.37e-06	6.08e-05	3.137e-04	3.87e-04	2.48e-04	1.357e-05
FTC-NFTSMC2-DPRL	4.686e-06	8.655e-05	3.278e-04	4.046e-04	4.094e-04	2.339e-05
Proposed FTC	2.966e-06	5.948e-05	3.179e-04	3.618e-04	3.221e-04	1.374e-05

Table 4. The mean absolute error of FTC-NFTSMC2-QPRL, FTC-NFTSMC2-DPRL, and Proposed in the simulation

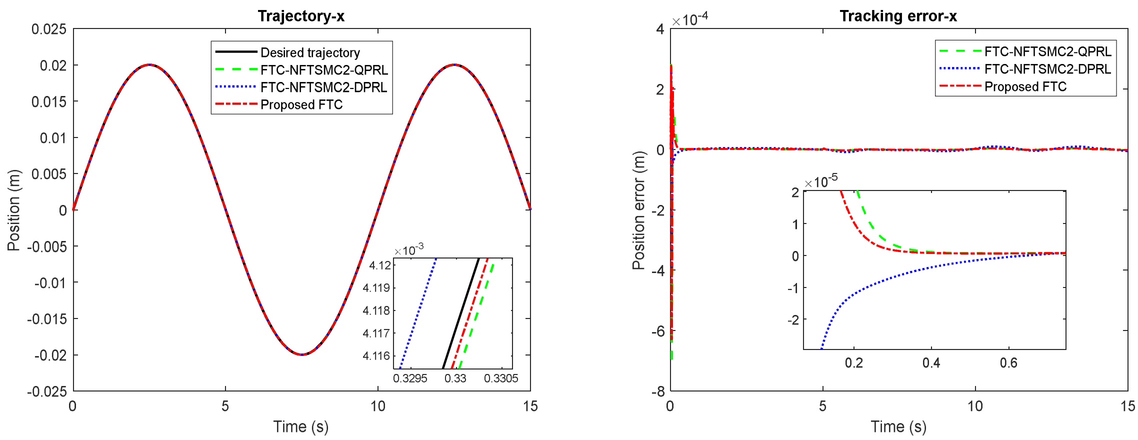

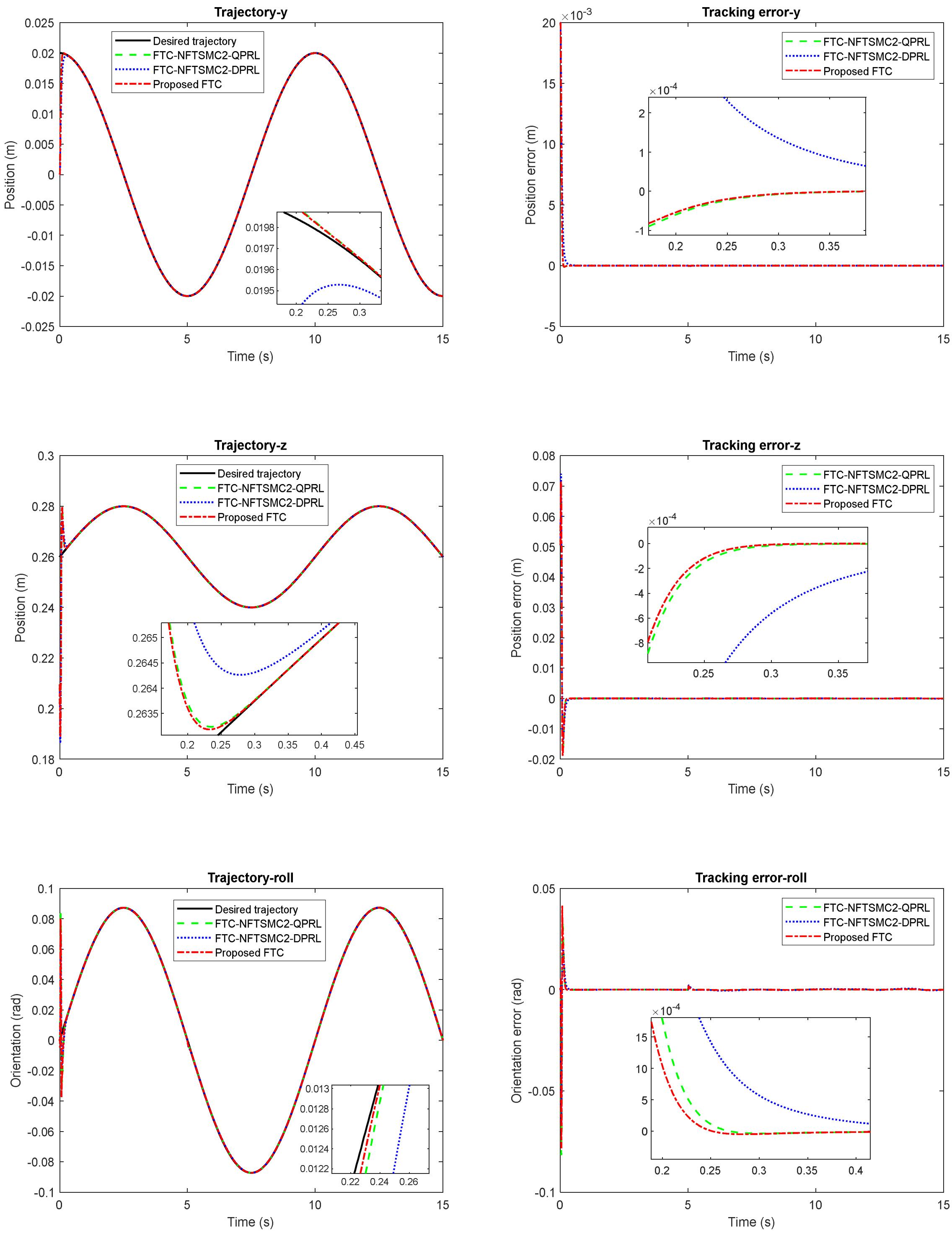

Trajectory-y
Desired trajectory
FTC-NFTSMC2-QPRL
FTC-NFTSMC2-DPRL
Proposed FTC
Position (m)
Time (s)
Tracking error-y
Position error (m)
Trajectory-z
Tracking error-z
Trajectory-roll
Orientation (rad)
Tracking error-roll
Orientation error (rad)

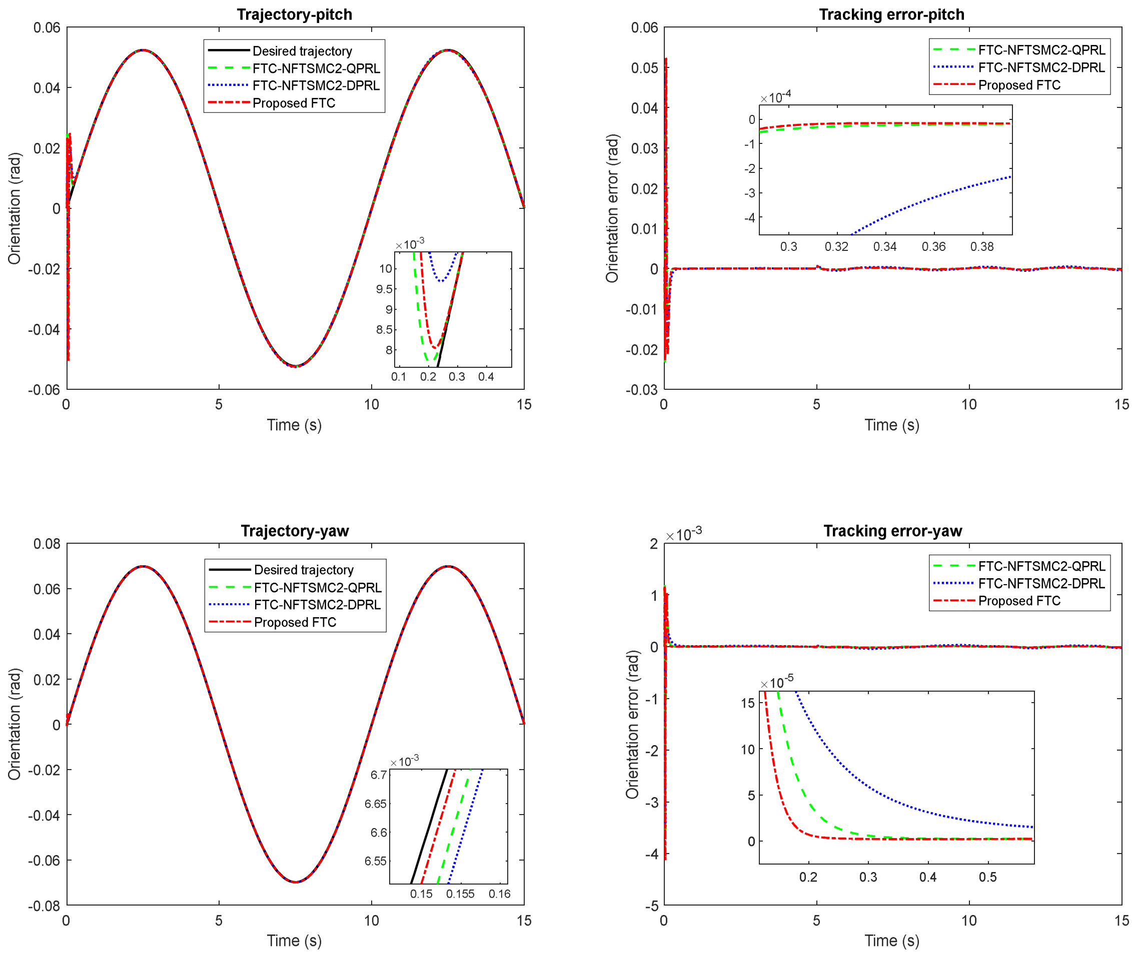

Figure 10. The tracking trajectory and performance of FTC-NFTSMC2-QPRL, FTC-NFTSMC2-DPRL, and Proposed FTC for the SP in the simulation

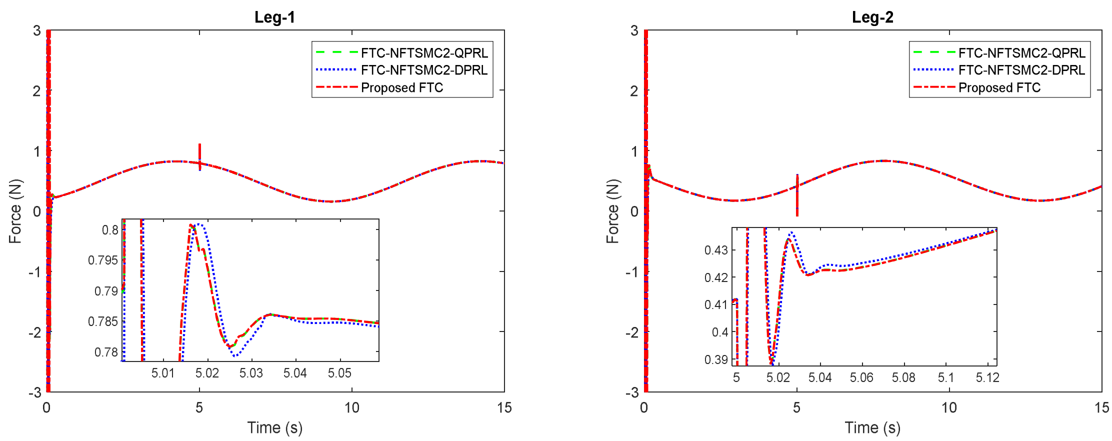

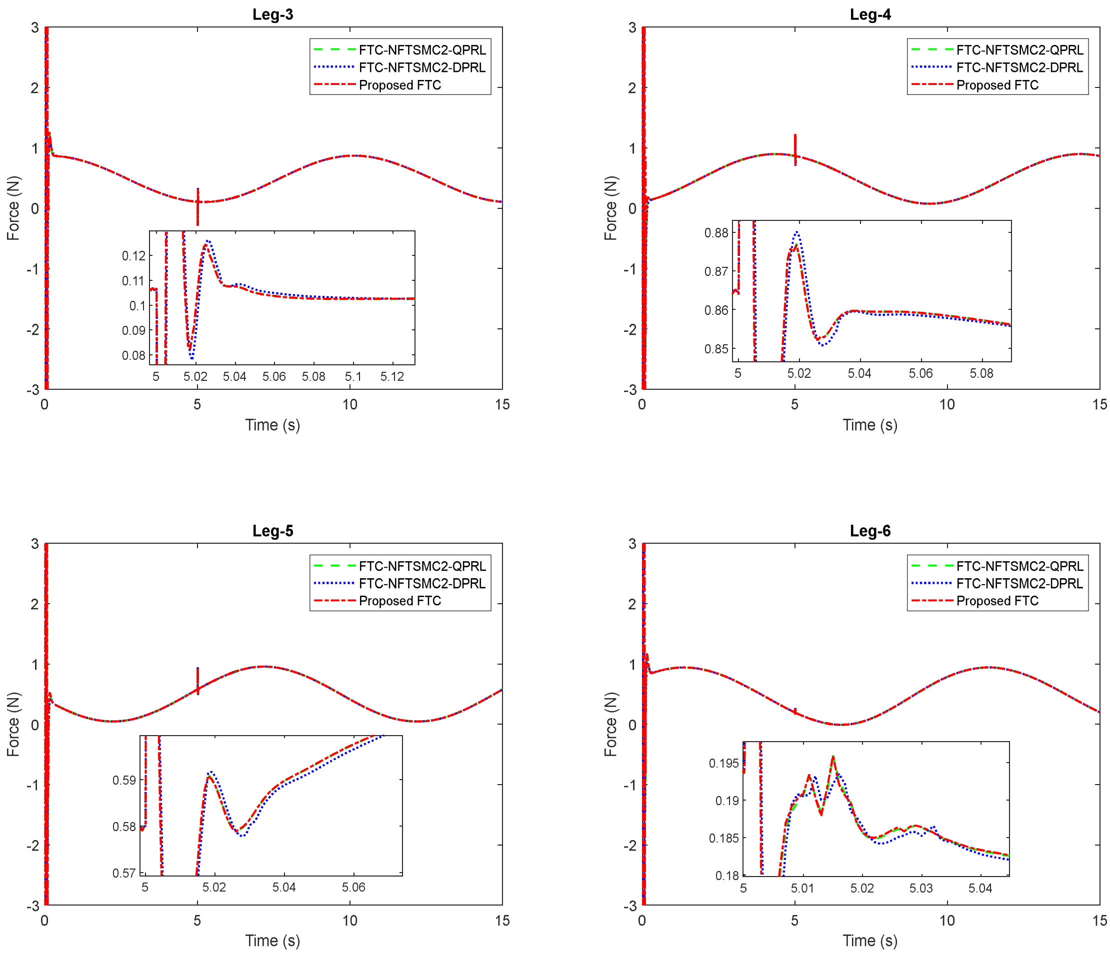

Figure 11. Input Force at each leg of the SP for FTC-NFTSMC2-QPRL, FTC-NFTSMC2-DPRL, and Proposed FTC in the simulation

3.2 Experiment results

This section describes implementations of the proposed FTC compared with the other controllers for an actual SP that was assembled with plastic upper and lower platforms and six MightyZap actuators (12Lf-17F-90; IR Robot Co., Ltd., Korea) shown in Figure 12. This actual SP was designed with parameters *c, b, d,* and e in Figure 1 set as 54 mm, 198 mm, 54 mm, and 126 mm, respectively.

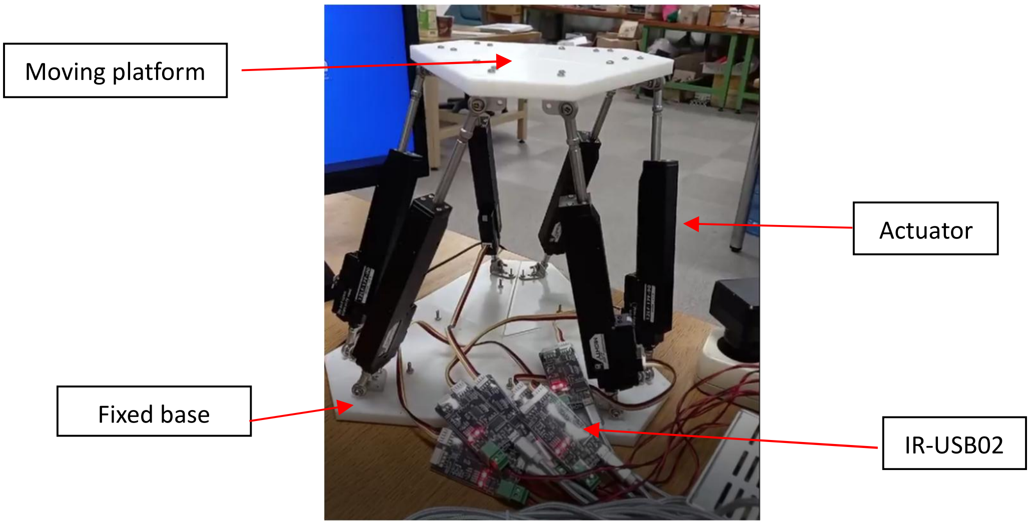

Figure 12. Actual Stewart Platform

The scheme of the system for controlling the Stewart Platform was built to realize the control process as shown in Figure 13.

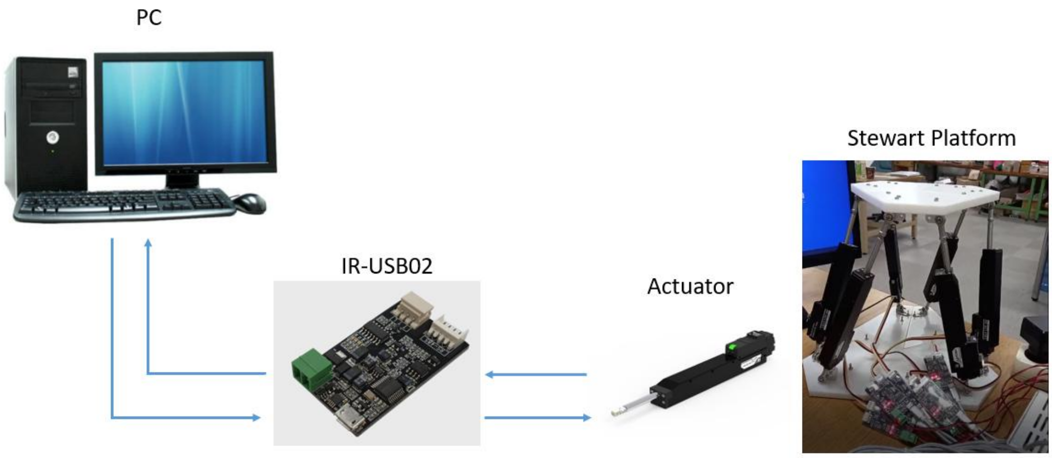

Figure 13. Scheme of the system

The reference trajectory of the upper platform was given in (38). The parameters of NFTSMC, FTC-NFTMSC1, Proposed FTC, ESO1, and ESO2 were set in Table 5.

Constants	NFTSMC	FTC-NFTSMC1	Proposed FTC
λ_1	0.1	0.1	0.1
λ_2	0.02	0.02	0.02
l/h	27/19	27/19	27/19

q/p	21/19	21/19	21/19
k_1	0.1	0.1	0.1
k_2	400	400	400
ε	0.1	0.1	0.1
c	0.2	0.2	0.2
η	0.1	0.1	0.1
r	1.1	1.1	1.1
α_1		3	1
α_2		3	1
α_3		1	
μ		0.09	0.09

Table 5. Parameters of three controllers NFTSMC, FTC-NFTSMC1, and Proposed FTC in the experiment

Next, we assumed that multiple faults occurred in the first, third, and fifth actuators from 5^{th} sec, as described in the Simulation section (VI above), and the torque functions with multiple faults were described in (7) where the parameters were set as in the Simulation section.

The tracking trajectory and performance of the NFTSMC, FTC-NFTSMC1, and Proposed FTC are illustrated in Figure 14 and Table 6. The performances of FTC-NFTSMC1 and Proposed FTC were slightly better than that of NFTSMC within the first five seconds. When actuator faults appeared after five seconds, the tracking errors of FTC-NFTSMC1 and Proposed FTC were considerably lower than those of NFTSMC due to the successful compensation of ESO1 and ESO2 for the disturbances, uncertainties, and faults. In addition, the peaking value in Proposed FTC was a little lower than that of FTC-NFTSMC1 when the fault occurred. It should be noted that the actual SP might have had different uncertainty and disturbance compared to the simulation, so the performance results of the actual SP were unlike those of the simulation. Overall, FTC-NFTSMC1 and Proposed FTC had smaller tracking errors than NFTSMC, while Proposed FTC achieved slightly higher accuracy than FTC-NFTSMC1. Figure 15 shows the control signals of three controllers. FTC-NFTSMC1 and Proposed FTC used ESO1 and ESO2 respectively to compensate for uncertainties, disturbances, and faults, while NFTSMC had no compensation for those. Hence, the controllers gave major differences in the input force at each joint.

Controllers	MAE x (m)	MAE y (m)	MAE z (m)	MAE roll (rad)	MAE pitch (rad)	MAE yaw (rad)
NFTSMC	0.0036	0.0044	0.0027	0.0071	0.0101	0.0199
FTC-NFTSMC1	0.0021	0.0019	0.0023	0.005	0.0064	0.0096
Proposed FTC	0.0018	0.0014	0.0021	0.0046	0.0052	0.0074

Table 6. The mean absolute error comparison of NFTSMC, FTC-NFTSMC1, and Proposed FTC in the experiment

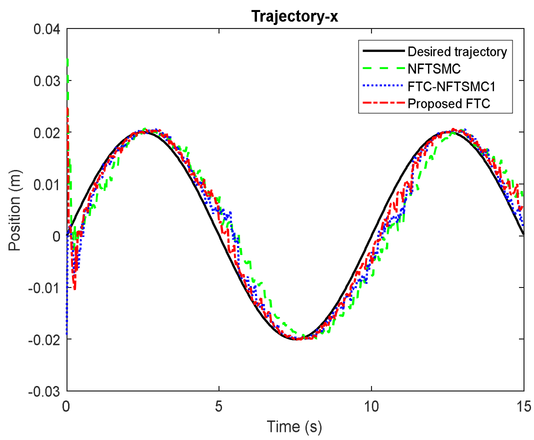

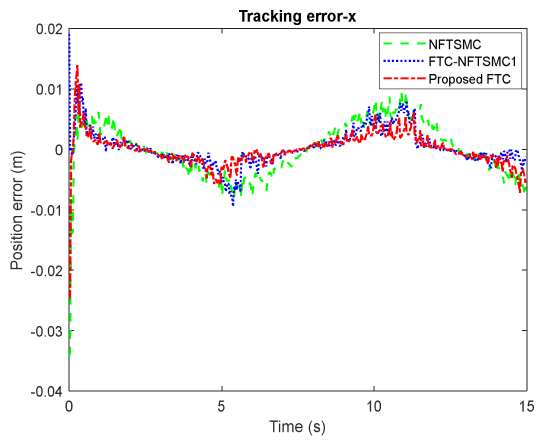

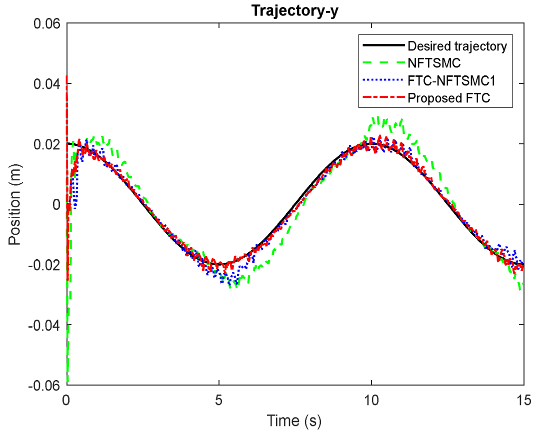
Trajectory-y
Position (m)
Time (s)
Desired trajectory
NFTSMC
FTC-NFTSMC1
Proposed FTC

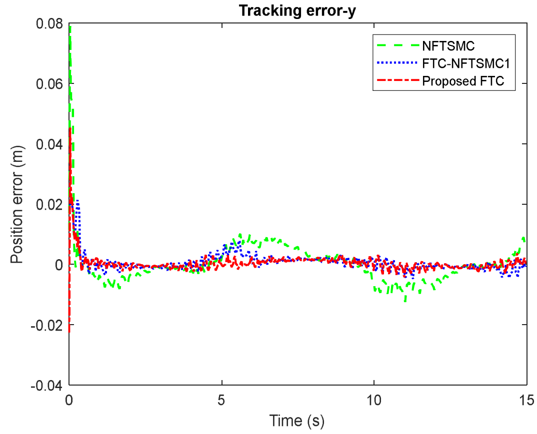
Tracking error-y
Position error (m)
Time (s)
NFTSMC
FTC-NFTSMC1
Proposed FTC

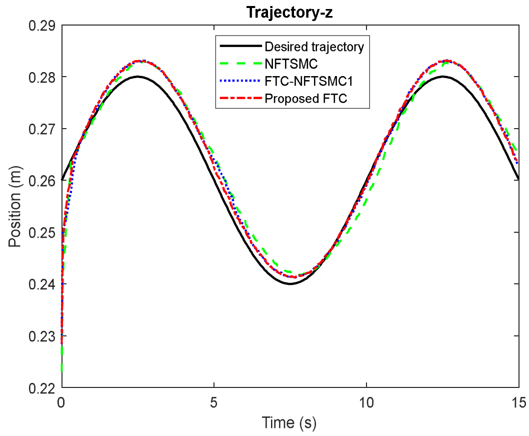
Trajectory-z
Position (m)
Time (s)
Desired trajectory
NFTSMC
FTC-NFTSMC1
Proposed FTC

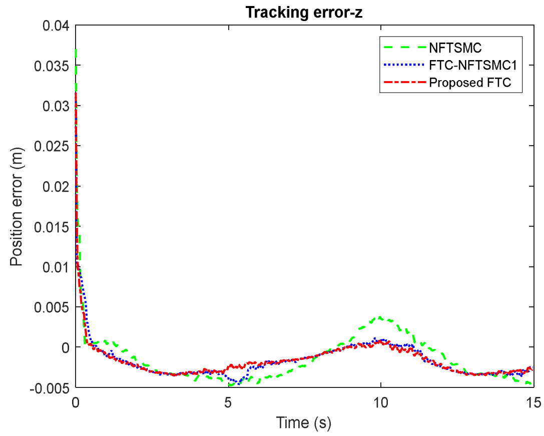
Tracking error-z
Position error (m)
Time (s)
NFTSMC
FTC-NFTSMC1
Proposed FTC

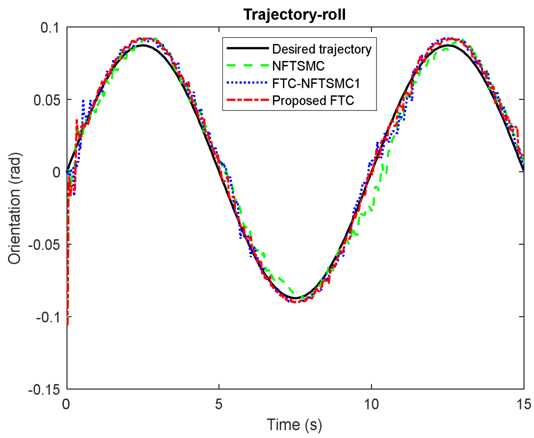
Trajectory-roll
Orientation (rad)
Time (s)
Desired trajectory
NFTSMC
FTC-NFTSMC1
Proposed FTC

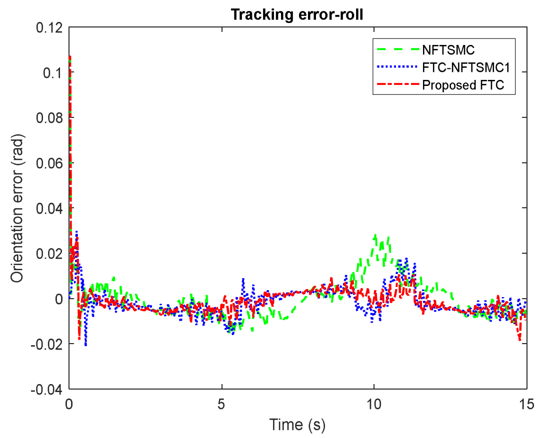
Tracking error-roll
Orientation error (rad)
Time (s)
NFTSMC
FTC-NFTSMC1
Proposed FTC

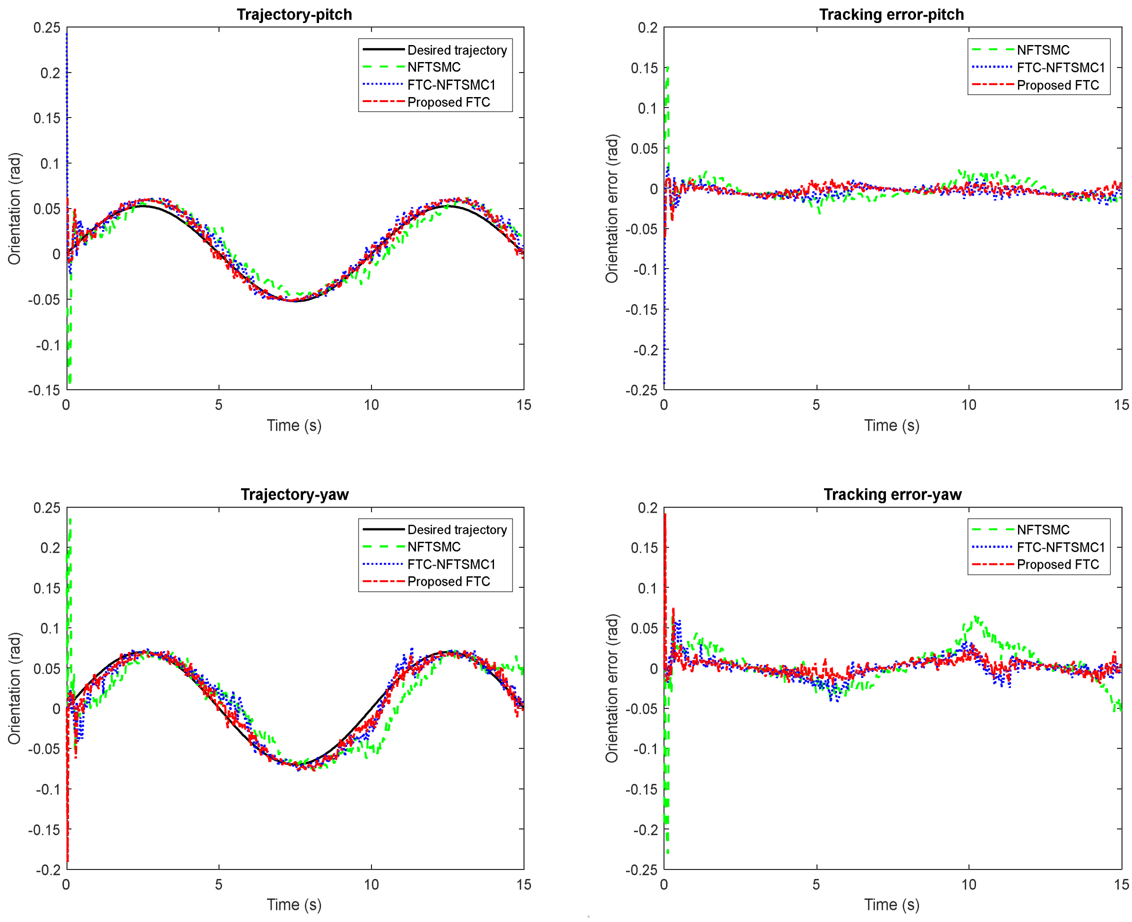

Figure 14. The tracking trajectory and performance of NFTSMC, FTC-NFTSMC1, and Proposed FTC for the actual SP in the experiment

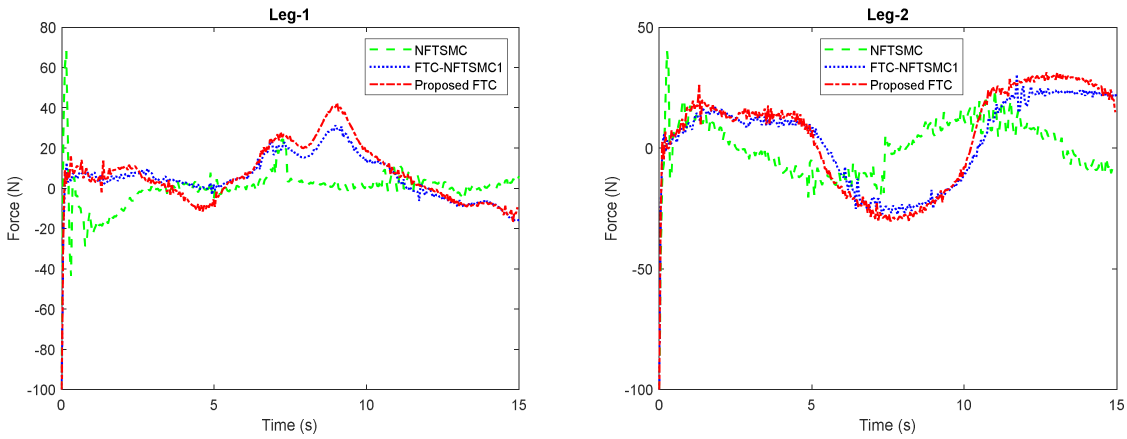

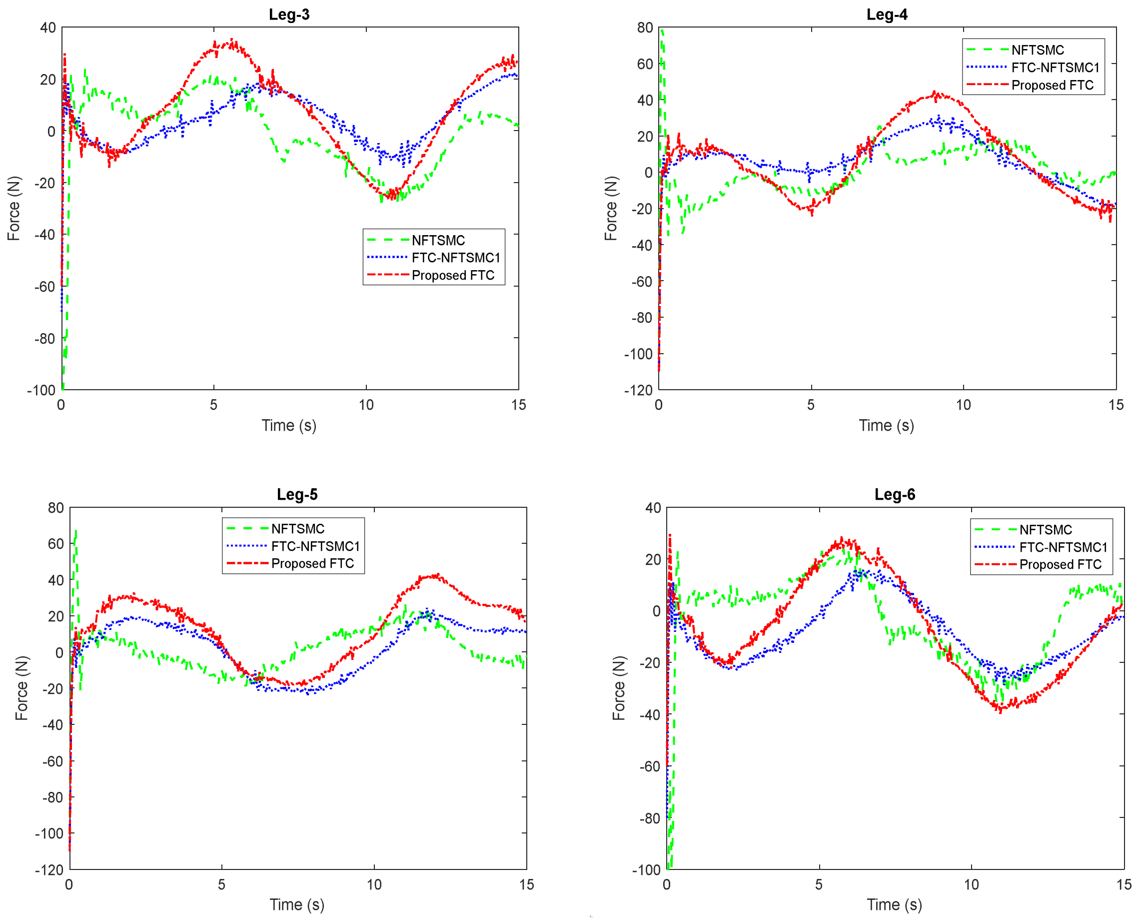

Figure 15. Input force at each leg of the actual SP for NFTSMC, FTC-NFTSMC1, and Proposed FTC in the experiment

To evaluate the efficiency of the proposed reaching law, we investigated the performance of FTC-NFTSMC2-QPRL (41), FTC-NFTSMC2-DPRL (42), and our Proposed FTC (28) in controlling the actual SP. The parameters of the three controllers were given in Table 7. Figure 16 and Table 8 show the performance of Proposed FTC compared with FTC-NFTSMC2-QPRL and FTC-NFTSMC2-DPRL. In general, the three controllers had similar performances in the presence of the actuator faults. Due to the noise in the practical system and possible limitations of response ability of the hardware, it was not as easy to clearly see the difference in the convergence speed of the controllers as it had been in the simulation. However, the simulation results showed the fast convergence rate of the proposed controller compared with the other controllers. It demonstrated that the proposed controller can obtain a fast convergence speed. On the other hand, the three controllers used the same ESO2 for the estimation and compensation, thus there were no significant differences in the magnitude of control signals at each leg shown in Figure 17.

Constants	FTC-NFTSMC2-QPRL	FTC-NFTSMC2-DPRL	Proposed FTC
λ_1	0.1	0.1	0.1
λ_2	0.02	0.02	0.02
l/h	27/19	27/19	27/19
q/p	21/19	21/19	21/19
k_1	0.1	0.1	0.1
k_2	400	400	400
ε	0.1	0.1	0.1
c	0.2	0.2	0.2
η	0.1	0.1	0.1
r			1.1
w_1	0.8	0.8	
w_2		1.1	

Table 7. Parameters of three controllers FTC-NFTSMC2-QPRL, FTC-NFTSMC2-DPRL, and Proposed FTC in the experiment

Controllers	MAE x (m)	MAE y (m)	MAE z (m)	MAE roll (rad)	MAE pitch (rad)	MAE yaw (rad)
FTC-NFTSMC2-QPRL	0.0018	0.0017	0.0022	0.0051	0.0065	0.0095
FTC-NFTSMC2-DPRL	0.0021	0.0017	0.0021	0.0057	0.0059	0.0099
Proposed FTC	0.0018	0.0014	0.0021	0.0046	0.0052	0.0074

Table 8. The mean absolute error comparison of FTC-NFTSMC2-QPRL, FTC-NFTSMC2-DPRL, and Proposed FTC in the experiment

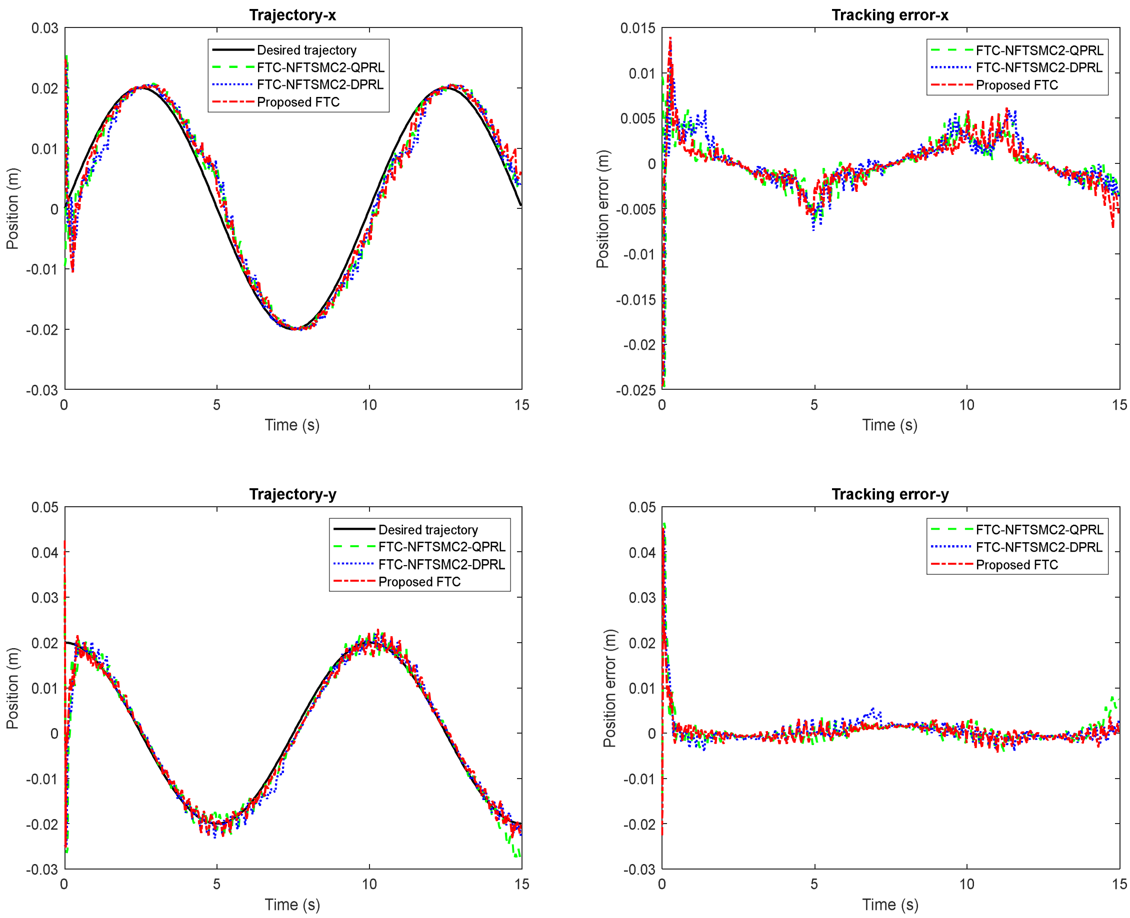

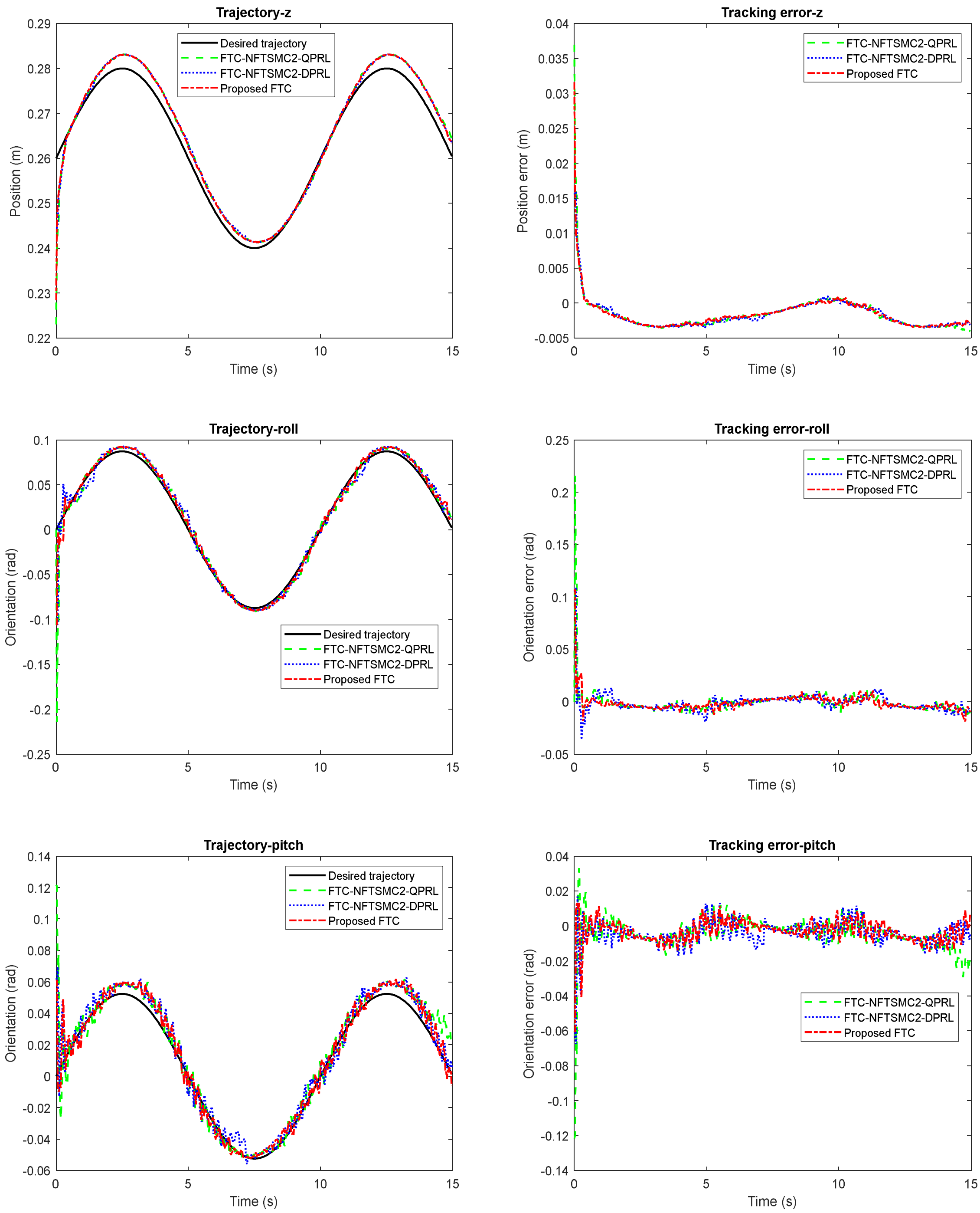
Trajectory-z
Position (m)
Time (s)
Desired trajectory
FTC-NFTSMC2-QPRL
FTC-NFTSMC2-DPRL
Proposed FTC
Tracking error-z
Position error (m)
Time (s)
FTC-NFTSMC2-QPRL
FTC-NFTSMC2-DPRL
Proposed FTC
Trajectory-roll
Orientation (rad)
Time (s)
Desired trajectory
FTC-NFTSMC2-QPRL
FTC-NFTSMC2-DPRL
Proposed FTC
Tracking error-roll
Orientation error (rad)
Time (s)
FTC-NFTSMC2-QPRL
FTC-NFTSMC2-DPRL
Proposed FTC
Trajectory-pitch
Orientation (rad)
Time (s)
Desired trajectory
FTC-NFTSMC2-QPRL
FTC-NFTSMC2-DPRL
Proposed FTC
Tracking error-pitch
Orientation error (rad)
Time (s)
FTC-NFTSMC2-QPRL
FTC-NFTSMC2-DPRL
Proposed FTC

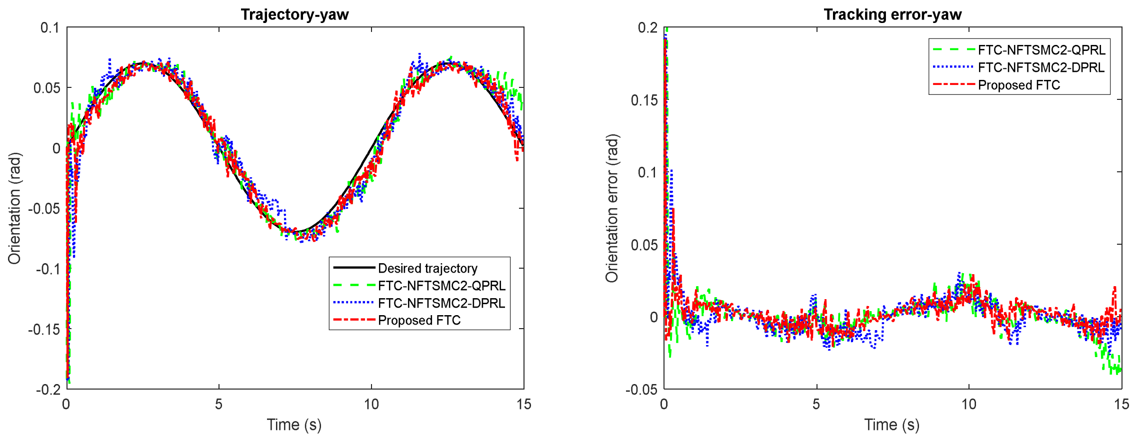

Figure 16. The tracking trajectory and performance of FTC-NFTSMC2-QPRL, FTC-NFTSMC2-DPRL, and Proposed FTC for the actual SP in the experiment

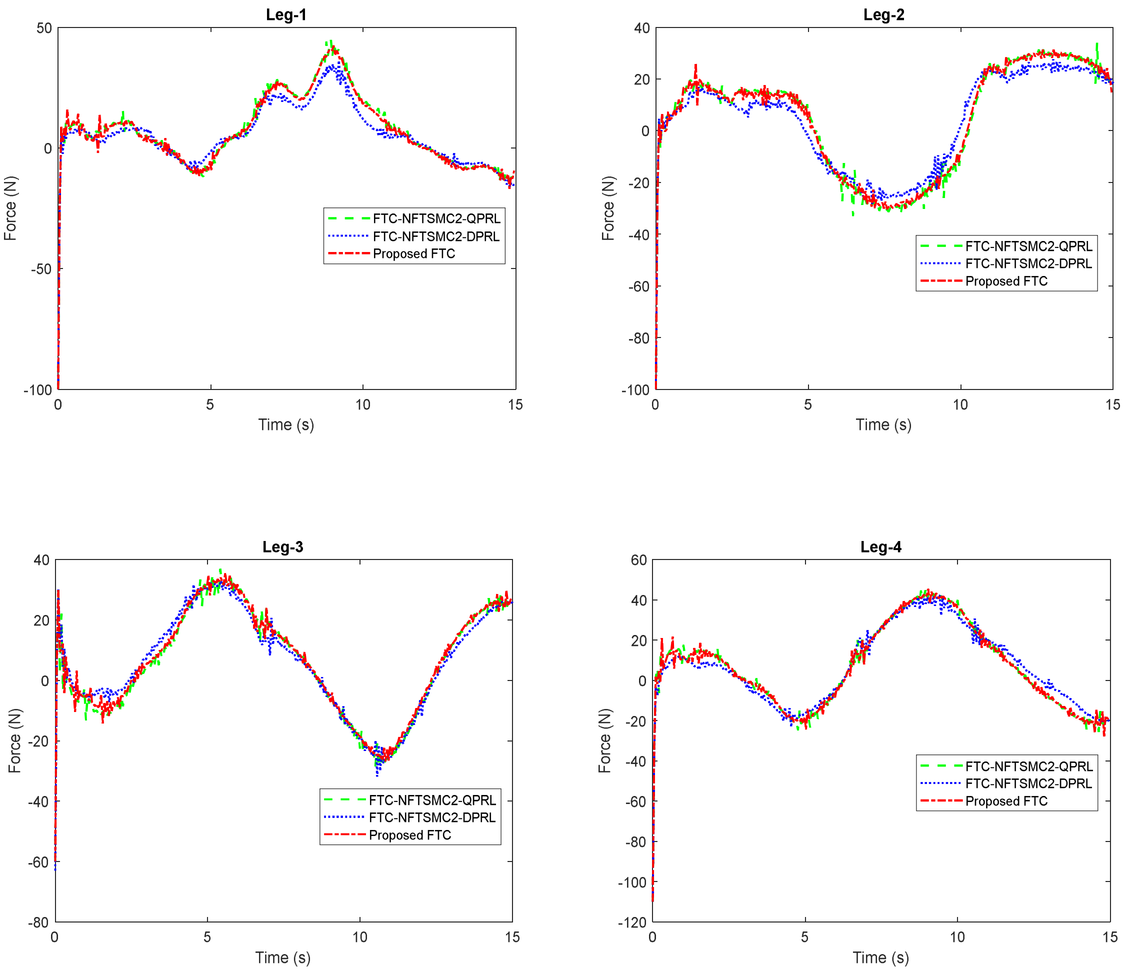

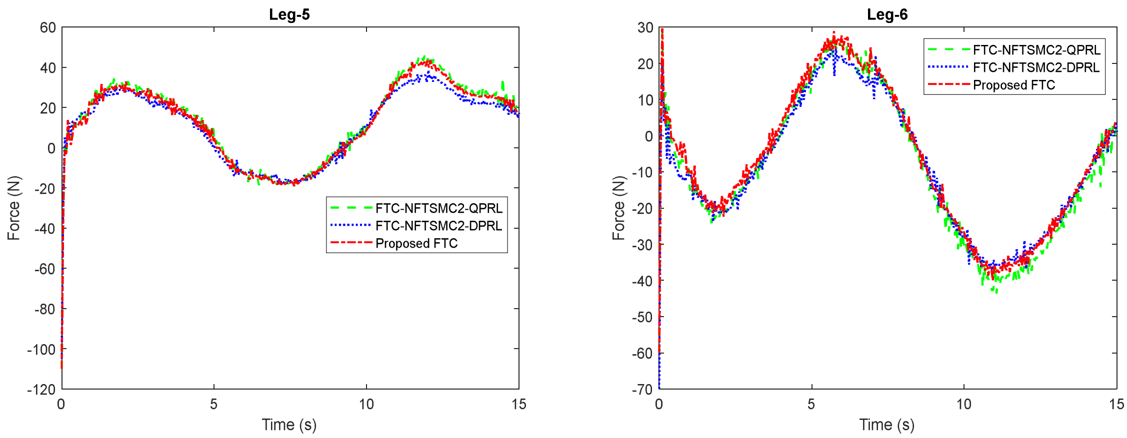

Figure 17. Input Force at each leg of the actual SP for FTC-NFTSMC2-QPRL, FTC-NFTSMC2-DPRL, and Proposed FTC in the experiment

4. FAULT-TOLERANT CONTROL FOR HAPTIC DEVICE IN TELEOPERATION

4.1 Introduction

Teleoperation is a popular technology in robotics that enable humans to control robots remotely. These days, teleoperation has been widely used to replace humans in many fields and hazardous environments such as surgery, deep water exploration, space exploration, and nuclear power plants.

Teleoperation includes a master device (haptic device), slave robot, and communication channels. The movement of the haptic device gives a position command sent to a slave robot. The feedback information such as interaction force and images are fed back to the master device. This is called bilateral teleoperation, which helps operators feel more realistic and enhance the user performance while doing a task. For example, considering a situation such as controlling a mobile robot, an operator moves the haptic handle to control the movement of the robot and the images showing the environment are sent to the operator. However, if the information are just images without depth information, it will be challenging for the user to prevent the robot from hitting obstacles. Therefore, depth information is required. When the robot approaches obstacles, it will give the force feedback rendered from the depth information to the operators through the haptic device. This feedback helps the operator notice that the robot is moving toward the obstacle. Hence, the development of a haptic device with feedback is necessary for the teleoperation system. There have been many investigations to advance haptic performance [39]–[42]. A haptic device based on an admittance control is a simple and efficient way that calculates a displacement corresponding to a force input. The relationship between the force and movement is imposed by a mass damper spring system. An admittance control often has two loops. The external loop as an admittance model is used to transform the force input into movements of a handle of the haptic device. The inner loop called position control is used to track the desired position given by the external loop. In the previous literature, the presence of faults was not considered in the haptic device, hence this research will apply the proposed FTC in subsection 2.5 for the inner position control of the haptic device based on the Stewart Platform. The proposed FTC will improve the performance of the haptic device and make the haptic handle move smoothly under the existence of actuator faults. Finally, the haptic device will be applied for controlling a mobile robot and receiving force feedback from the robot to help the operator avoid the collision and enhance the task performance

4.2 Admittance model

The structure of the haptic device is shown in Figure 18. Haptic device based on Stewart Platform which includes some main components such as a Stewart Platform, a force/torque sensor (F/T sensor) RFT80-6A01 (ROBOTOUS Co,. Ltd., Korea) is mounted on the upper platform, and a handle is mounted on the F/T sensor. The admittance model regulates the relationship between the movement of the haptic handle and a contact force on the handle. The admittance equation for 1-DOF is described as

$$\frac{x_r(s)}{F(s)} = \frac{1}{M_i s^2 + B_i s + K_i} \tag{43}$$

where F is the force impacting on the handle, x_r represents the position of the haptic handle in task space. M_i, B_i, and K_i are Cartesian inertia, viscosity, and stiffness of the mechanical system, respectively

For a 6-DOF haptic device, x_r has six elements described as

$$\begin{bmatrix} p_x \\ p_y \\ p_z \\ \varphi_x \\ \varphi_y \\ \varphi_z \end{bmatrix} = \frac{1}{M_i s^2 + B_i s + K_i} \begin{bmatrix} f_x \\ f_y \\ f_z \\ m_x \\ m_y \\ m_z \end{bmatrix} \tag{44}$$

where p_x, p_y, and p_z are the position of the haptic handle. φ_x, φ_y, and φ_z are the orientation of the haptic handle. f_x , f_y , and f_z are the force measured by the force/torque sensor. m_x, m_y, and m_z are the torque measured from the force/torque sensor.

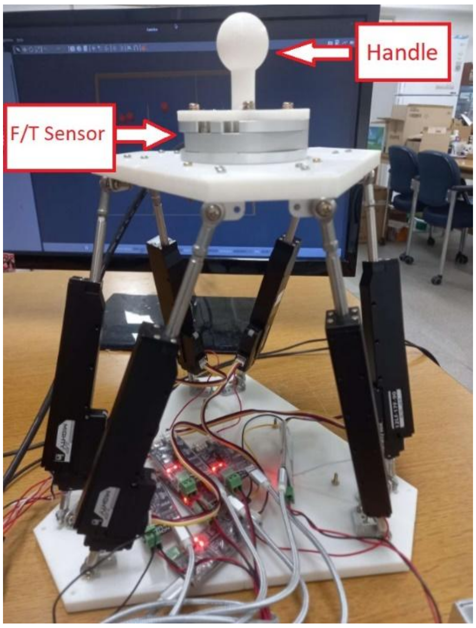

Figure 18. Haptic device based on Stewart Platform

4.3 Experiment

4.3.1 The performance of the proposed FTC for the haptic device

The haptic device shown in Figure 18 is built by the Stewart Platform using the admittance model (44) for the external loop control and the proposed FTC (28) for the inner position control. The random movements of the upper platform were given by the force impacting on the handle through the admittance model (44) where $M_i = 1$, $B_i = 70$, $K_i = 800$. The proposed FTC (28) controls the haptic device to track the reference trajectory resulting from (44). To test the robustness of the proposed FTC (28) compared with NFTSMC without ESO (NFTSMC) (39) and NFTSMC with the standard ESO1 (FTC-NFTSMC1), it was assumed that faults occur at leg 2, leg 4, and leg 6 from the tenth second. The torque functions of actuators with the existence of faults were defined in (7) where the gain faults can be assumed as $\rho_1(t)=0$, $\rho_2(t)=0.2+0.3\sin(\pi t)$, $\rho_3(t)=0$, $\rho_4(t)=0.3+0.1\cos(3t+2)$, $\rho_5(t)=0$, $\rho_6(t)=0.25+0.2\cos(t+7)$ and the bias faults can be assumed as $f_1(t)=0$, $f_2(t)=0.3\cos(0.5t+10)$, $f_3(t)=0$, $f_4(t)=0.2\sin(3t)$, $f_5(t)=0$, and $f_6(t)=\sin(t+5)$. The parameters of ESO1, ESO2, controllers NFTSMC, FTC-NFTSMC1, and Proposed FTC are set as in Table 5.

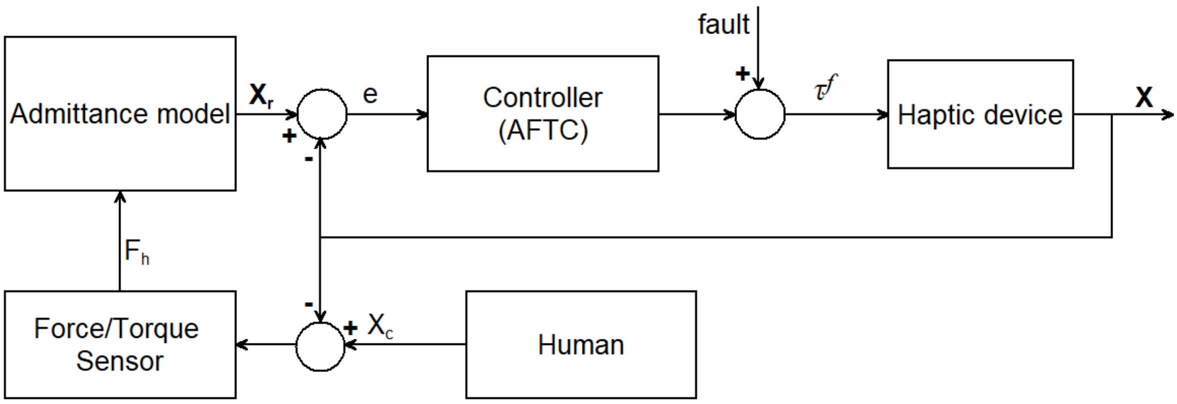

Figure 19. Human-haptic device cooperation scheme

For the teleoperation of a mobile robot, just two degrees of freedom (DOF) of Stewart platform are used. Thus, we considered the performance of x and y directions only, and neglected the remaining DOFs in this study. Figure 20 and Table 9 show experimental results of the haptic device using NFTSMC, FTC- NFTSMC1, and Proposed FTC for x and y directions. It can be seen that the performance of FTC- NFTSMC1 and Proposed FTC were better than NFTSMC in the first ten seconds due to the estimation and compensation of ESO1 and ESO2 in the control laws for unknown uncertainties and disturbances of the system. Next, after ten seconds, the actuator faults occurred and the controllers showed significantly different performances. Thanks to the compensation of ESO1 and ESO2, FTC- NFTSMC1 and Proposed FTC presented superior performance compared to NFTSMC for control tasks even though the faults arose. Proposed FTC using ESO2 was a bit more effective than FTC-NFTSMC1. Besides, the haptic handle using NFTSMC did not move smoothly under the presence of faults, which caused uncomfortable for the operator. In summary, the haptic device using Proposed FTC had high precision and moved smoothly compared with the other controllers.

	NFTSMC	FTC-NFTSMC1	Proposed FTC
MAE-x	0.0026	0.0016	0.0015
MAE-y	0.0024	0.0014	0.0012

Table 9. The mean absolute errors of the haptic device for x and y directions

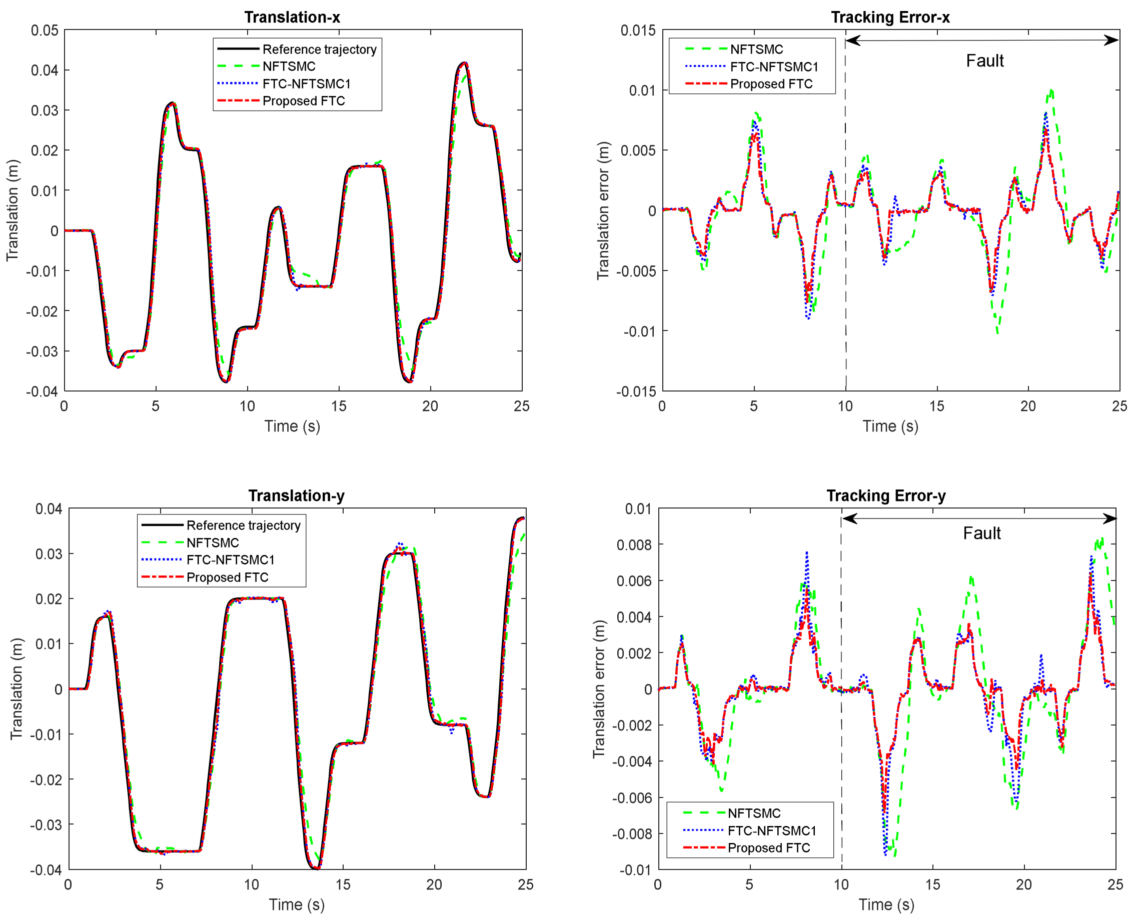

Figure 20. The performance of the haptic device using NTSMC, FTC-NFTSMC1, and Proposed FTC

4.3.2 Teleoperation of a mobile robot in the virtual environment

Figure 21 shows the cooperation between humans and haptic device for teleoperation. The proposed haptic device with the faulty assumption in subsection 4.3.1 was tested for teleoperation in the virtual environment built in Gazebo and shown in Figure 22. The virtual environment includes a mobile robot and obstacles. The mobile robot is equipped with a Lidar sensor to detect obstacles. The laser scanner provides an angular solution of 1 degree, an angular range of 360 degrees, and a distance range of approximately 3.5 m at a scan rate of approximately 300rpm. The obstacles have different shapes and sizes, and are comprised of cylinders, cubes, and walls. The haptic device was connected to the computer and communicated with the mobile robot via ROS (Robot Operating System) software platform. According to [42], a logical position of the haptic handle can be mapped to the motion parameters of the mobile robot. For this research, the position commands x and y were mapped to the speed rate and turning rate shown in Figure 23, respectively. In this experiment, the operator remotely controls the mobile robot by moving the haptic handle. The mission is that the operator controls the mobile robot to move from the start point to the goal point as fast as possible while simultaneously avoiding the obstacles on the given route shown in Figure 22.

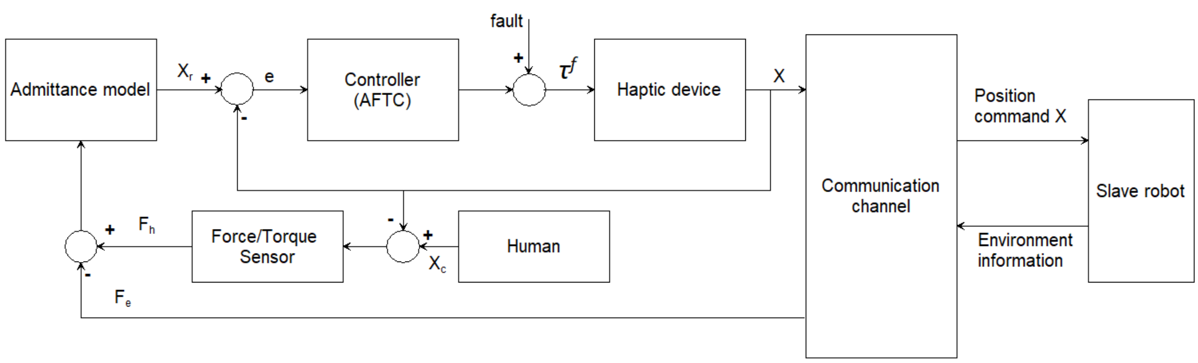

Figure 21. Human-haptic device for teleoperation of a mobile robot

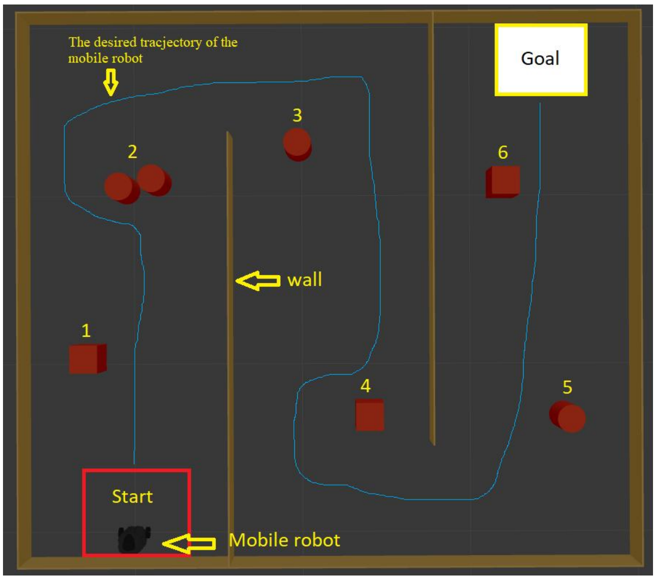

Figure 22. A mobile robot in a virtual environment

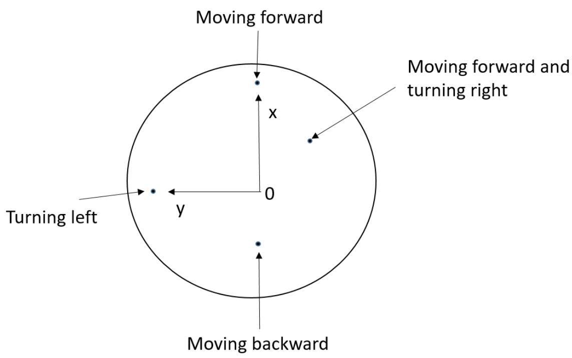

Figure 23. Mapping a logical point (x, y) to motion parameters (speed rate, turning rate)

The position of the haptic handle and contact force on the handle measured by the force/torque sensor are shown in Figure 24. Due to the measurement noise and the sensitivity of the F/T sensor, there were contact force oscillations lower than 5N in Figure 24.b, but it did not cause difficulty in controlling the haptic handle. It took approximately 145s to complete the mission and the robot approached the obstacles two times. When the robot closed to obstacles two and four, the force feedback was provided to the haptic device to drive the handle backward at the 16th and 83rd seconds, which made the contact force increase and the robot move away from the obstacles. In the real field, this would protect the robot from damage due to an unexpected collision. These results illustrated the adequacy and effectiveness of the proposed haptic device for the teleoperation of a mobile robot.

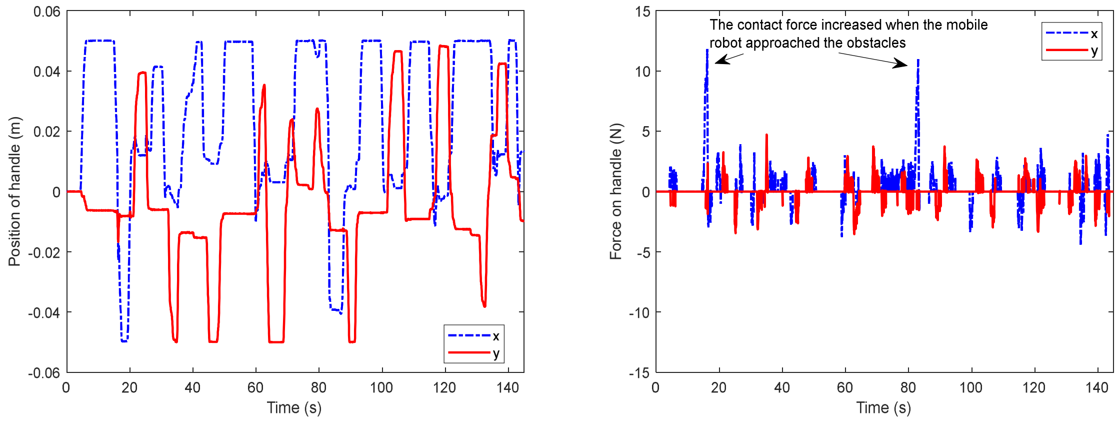

a) b)

Figure 24**.** Experimental results of teleoperation. a) Movement of the haptic handle to control a mobile robot. b) Contact force on the haptic handle

5. CONCLUSION

In this study, a new fault-tolerant scheme was proposed for a Stewart platform. First, a NFTSMC was used in the FTC to enhance the convergence speed of the state in finite time without the singularity issue. Then ESO2 was applied for the FTC to not only effectively estimate and compensate for the uncertainty, disturbances, and faults, but also reduce the peaking issue in the conventional ESO1. To further enhance the reaching phase speed and decrease the chattering, an improved reaching law (15) was designed and its quick convergence ability in finite time was demonstrated. Consequently, the new FTC showing the above benefits was derived by combining the NFTSMC, the ESO2, and the novel reaching law (15). To assess the efficiency of the proposed FTC, the desired trajectory and an assumption of faults were used for all the controllers throughout the simulation and experiments. Next, we showed a comparison between the proposed FTC and the control law using the traditional ESO1 and the control law without the ESO to evaluate the effectiveness of ESO2 in the FTC scheme. Then, the performance of the proposed FTC and the other FTC schemes using the same ESO2 but different reaching laws are exhibited to demonstrate enhancement in the convergence rate of the NRL. By verifying the simulation and the experiments, we could confirm that the proposed FTC is easy to implement and has the inherent advantages of the NFTSMC, the estimation and compensation ability of ESO2 plus the reaching speed improvement of the improved reaching law (15). Thus, the proposed FTC showed remarkable features such as insensitivity to uncertainties, disturbances, and faults, reducing the peaking value, high precision and robustness, rejecting the singularity, less oscillation, and a fast convergence speed in finite time. Accordingly, the development of a haptic device based on Stewart platform using the admittance model and the proposed fault-tolerant control was presented. The admittance model was used to convert force input to the handle position. The position control based on the proposed fault-tolerant algorithm was used to track the desired position given by the admittance model. Proposed FTC illustrated the robustness trait and improved the stability of the haptic device even though unknown disturbances and faults appeared in the system. Additionally, the haptic device using Proposed FTC moved smoother than the haptic device using the other controllers which makes the operator comfortable in controlling the haptic handle. Finally, the teleoperation of a mobile robot in a virtual environment was implemented to assess the proposed haptic device. The results demonstrated that the proposed master device was effective for the teleoperation of the mobile robot.

6. LIMITATIONS AND FUTURE WORKS

Limitations:

In this study, the dynamic model of the system must be known. However, in practice, it is difficult to obtain the dynamic models of various systems. Besides, there are many parameters in the control law and the selection of the parameter is really strict, which are mainly tuned by the trial-and-error method, in a real-time system is really not a trivial task.

Future works:

The estimation for the dynamic model needs to be studied. A method should be investigated to automatically tune both the estimation and control gains.

PUBLICATIONS

International Journal

[1] D.-V. Le and C. Ha, "Finite-time Fault-Tolerant Control for a Stewart Platform using Sliding Mode Control with Improved Reaching Law," *IEEE Access*, vol. 10, pp. 1–1, 2022, doi: 10.1109/access.2022.3165091.

International Conferences

[2] D.-V. Le and C. Ha, "Application of Stewart Platform as a haptic device for teleoperation of a mobile robot", accepted in 2022 International Conference on Intelligent Computing, Xi'an, China, August 7-11, 2022

REFERENCE

[1] J. P. Merlet, *Parallel robots*, vol. 128. 2006.

[2] N. Leroy, A. M. Kökösy, and W. Perruquetti, "Dynamic modeling of a parallel robot. Application to a surgical simulator," *Proc. - IEEE Int. Conf. Robot. Autom.*, vol. 3, pp. 4330–4335, 2003, doi: 10.1109/robot.2003.1242270.

[3] Y. X. Su, B. Y. Duan, B. Peng, and R. D. Nan, "Singularity analysis of fine-tuning Stewart platform for large radio telescope using genetic algorithm," *Mechatronics*, vol. 13, no. 5, pp. 413–425, 2003, doi: 10.1016/S0957-4158(01)00051-4.

[4] G. Lebret, K. Liu, and F. L. Lewis, "Kinematic analysis of a stewart platform manipulator," *J. Robot. Syst.*, vol. 10, no. 5, pp. 629–655, 1993, doi: 10.1002/rob.4620100506.

[5] Q. Wang, *Closed form direct kinematics of a class of Stewart platform*, vol. 15, no. 1. IFAC, 2002.

[6] J. P. Merlet, "Direct Kinematics and Assembly Modes of Parallel Manipulators," *Int. J. Rob. Res.*, vol. 11, no. 2, pp. 150–162, 1992, doi: 10.1177/027836499201100205.

[7] P. Nanua and K. J.Waldron, "Direct Kinematic Solution of a Stewart Platform."

[8] Z. Geng and L. Haynes, "Neural network solution for the forward kinematics problem of a Stewart platform," *Proceedings. 1991 IEEE Int. Conf. Robot. Autom.*, 1991, doi: 10.1109/ROBOT.1991.132029.

[9] C. Yang, Q. Huang, P. O. Ogbobe, and J. Han, "Forward kinematics analysis of parallel robots using global Newton-Raphson method," *2009 2nd Int. Conf. Intell. Comput. Technol. Autom. ICICTA 2009*, vol. 3, pp. 407–410, 2009, doi: 10.1109/ICICTA.2009.564.

[10] Z. Geng, L. S. Haynes, J. D. Lee, and R. L. Carroll, "On the dynamic model and kinematic analysis of a class of Stewart platforms," *Rob. Auton. Syst.*, vol. 9, no. 4, pp. 237–254, 1992, doi: 10.1016/0921-8890(92)90041-V.

[11] L. W. Tsai, "Solving the inverse dynamics of a Stewart-Gough manipulator by the principle of virtual work," *J. Mech. Des. Trans. ASME*, vol. 122, no. 1, pp. 3–9, 2000, doi: 10.1115/1.533540.

[12] B. Dasgupta and T. S. Mruthyunjaya, "Closed-form dynamic equations of the general Stewart platform through the Newton-Euler approach," *Mech. Mach. Theory*, vol. 33, no. 7, pp. 993–1012, 1998, doi: 10.1016/S0094-114X(97)00087-6.

[13] Q. Meng, T. Zhang, J. F. He, and J. Y. Song, "Adaptive vector sliding mode fault-Tolerant control of the uncertain Stewart platform based on position measurements only," *Robotica*, vol. 34, no. 6, pp. 1297–1321, 2014, doi: 10.1017/S0263574714002276.

[14] J. Ma, T. Yang, Z. G. Hou, and M. Tan, "Neural network disturbance observer based controller of an electrically driven Stewart platform using backstepping for active vibration isolation," *Proc. Int. Jt. Conf. Neural Networks*, pp. 1939–1944, 2009, doi: 10.1109/IJCNN.2009.5179041.

[15] W. Qiang, C. Juan, and T. Zhiyong, "Study of sliding mode control for stewart platform based on simplified dynamic model," *IEEE Int. Conf. Ind. Informatics*, pp. 889–892, 2008, doi: 10.1109/INDIN.2008.4618227.

[16] L. Yang and J. Yang, "Nonsingular fast terminal sliding-mode control for nonlinear dynamical

systems," *Int. J. Robust Nonlinear Control*, no. November 2010, p. 23, 2015, doi: 10.1002/rnc.1666.

[17] S. S. D. Xu, C. C. Chen, and Z. L. Wu, "Study of nonsingular fast terminal sliding-mode fault-tolerant control," *IEEE Trans. Ind. Electron.*, vol. 62, no. 6, pp. 3906–3913, 2015, doi: 10.1109/TIE.2015.2399397.

[18] H. Wang, W. Bai, and P. X. Liu, "Finite-time adaptive fault-tolerant control for nonlinear systems with multiple faults," *IEEE/CAA J. Autom. Sin.*, vol. 6, no. 6, pp. 1417–1427, 2019, doi: 10.1109/JAS.2019.1911765.

[19] M. Van, M. Mavrovouniotis, and S. S. Ge, "An adaptive backstepping nonsingular fast terminal sliding mode control for robust fault tolerant control of robot manipulators," *IEEE Trans. Syst. Man, Cybern. Syst.*, vol. 49, no. 7, pp. 1448–1458, 2019, doi: 10.1109/TSMC.2017.2782246.

[20] Q. Shen, B. Jiang, and V. Cocquempot, "Adaptive Fuzzy Observer-Based Active Fault-Tolerant Dynamic Surface Control for a Class of Nonlinear Systems With Actuator Faults," *IEEE Trans. FUZZY Syst.*, vol. 22, no. 2, pp. 338–349, 2014, doi: 10.1109/TFUZZ.2013.2254493.

[21] B. Li, K. Qin, B. Xiao, and Y. Yang, "Finite-time Extended State Observer based fault tolerant output feedback control for attitude stabilization," *ISA Trans.*, vol. 91, pp. 11–20, 2019, doi: 10.1016/j.isatra.2019.01.039.

[22] C. Edwards, S. K. Spurgeon, and R. J. Patton, "Sliding mode observers for fault detection and isolation," *Automatica*, vol. 36, no. 4, pp. 541–553, 2000, doi: 10.1016/S0005-1098(99)00177-6.

[23] K. K. Hassan and Praly Laurent, "High-gain observers in nonlinear feedback control," *Int. J. Robust Nonlinear Control*, no. July 2013, p. 23, 2015, doi: 10.1002/rnc.3051.

[24] J. H. Ahrens and H. K. Khalil, "High-gain observers in the presence of measurement noise: A switched-gain approach," *Automatica*, vol. 45, no. 4, pp. 936–943, 2009, doi: 10.1016/j.automatica.2008.11.012.

[25] L. B. Freidovich and H. K. Khalil, "Performance recovery of feedback-linearization-based designs," *IEEE Trans. Automat. Contr.*, vol. 53, no. 10, pp. 2324–2334, 2008, doi: 10.1109/TAC.2008.2006821.

[26] M. Ran, Q. Wang, C. Dong, and L. Xie, "Active disturbance rejection control for uncertain time-delay nonlinear systems," *Automatica*, vol. 112, no. 11, pp. 5830–5836, 2020, doi: 10.1016/j.automatica.2019.108692.

[27] M. Ran, J. Li, and L. Xie, "A new extended state observer for uncertain nonlinear systems," *Automatica*, vol. 131, p. 109772, 2021, doi: 10.1016/j.automatica.2021.109772.

[28] M. S. Chen, Y. R. Hwang, and M. Tomizuka, "A state-dependent boundary layer design for sliding mode control," *IEEE Trans. Automat. Contr.*, vol. 47, no. 10, pp. 1677–1681, 2002, doi: 10.1109/TAC.2002.803534.

[29] H. M. Chen, J. C. Renn, and J. P. Su, "Sliding mode control with varying boundary layers for an electro-hydraulic position servo system," *Int. J. Adv. Manuf. Technol.*, vol. 26, no. 1–2, pp. 117–123, 2005, doi: 10.1007/s00170-004-2145-0.

[30] V. Utkin, "Discussion Aspects of High-Order Sliding Mode Control," *IEEE Trans. Automat. Contr.*, vol. 61, no. 3, pp. 829–833, 2016, doi: 10.1109/TAC.2015.2450571.

[31] J. J. Rath, M. Defoort, H. R. Karimi, and K. C. Veluvolu, "Output Feedback Active Suspension Control With Higher Order Terminal Sliding Mode," *IEEE Trans. Ind. Electron.*, vol. 64, no. 2,

pp. 1392–1403, 2017.

[32] W. Gao and J. C. Hung, "Variable Structure Control of Nonlinear Systems: A New Approach," *IEEE Trans. Ind. Electron.*, vol. 40, no. 1, pp. 45–55, 1993, doi: 10.1109/41.184820.

[33] T. Wang, M. Zhao, Y. Li, and K. Liu, "Double-power reaching law sliding mode control for spacecraft decline based on radial basis function networks," *Proc. 29th Chinese Control Decis. Conf. CCDC 2017*, pp. 5396–5401, 2017, doi: 10.1109/CCDC.2017.7979456.

[34] M. Tao, Q. Chen, X. He, and M. Sun, "Adaptive fixed-time fault-tolerant control for rigid spacecraft using a double power reaching law," *Int. J. Robust Nonlinear Control*, vol. 29, no. 12, pp. 4022–4040, 2019, doi: 10.1002/rnc.4593.

[35] C. J. Fallaha, M. Saad, H. Y. Kanaan, and K. Al-Haddad, "Sliding-mode robot control with exponential reaching law," *IEEE Trans. Ind. Electron.*, vol. 58, no. 2, pp. 600–610, 2011, doi: 10.1109/TIE.2010.2045995.

[36] G. Y. Yang and S. Y. Chen, "Piecewise fast multi-power reaching law: Basis for sliding mode control algorithm," *Meas. Control (United Kingdom)*, vol. 53, no. 9–10, pp. 1929–1942, 2020, doi: 10.1177/0020294020964246.

[37] Y. Li and S. Tong, "Adaptive neural networks decentralized ftc design for nonstrict-feedback nonlinear interconnected large-scale systems against actuator faults," *IEEE Trans. Neural Networks Learn. Syst.*, vol. 28, no. 11, pp. 2541–2554, 2017, doi: 10.1109/TNNLS.2016.2598580.

[38] B. Z. Guo and Z. L. Zhao, "On the convergence of an extended state observer for nonlinear systems with uncertainty," *Syst. Control Lett.*, vol. 60, no. 6, pp. 420–430, 2011, doi: 10.1016/j.sysconle.2011.03.008.

[39] A. Abdossalami and S. Sirouspour, "Adaptive control for improved transparency in haptic simulations," *IEEE Trans. Haptics*, vol. 2, no. 1, pp. 2–14, 2009, doi: 10.1109/TOH.2008.18.

[40] H. Park and J. M. Lee, "Adaptive impedance control of a haptic interface," *Mechatronics*, vol. 14, no. 3, pp. 237–253, 2004, doi: 10.1016/S0957-4158(03)00040-0.

[41] U. J. Na, "A new impedance force control of a haptic teleoperation system for improved transparency," *J. Mech. Sci. Technol.*, vol. 31, no. 12, pp. 6005–6017, 2017, doi: 10.1007/s12206-017-1145-6.

[42] C. Ju and H. Il Son, "Evaluation of Haptic Feedback in the Performance of a Teleoperated Unmanned Ground Vehicle in an Obstacle Avoidance Scenario," *Int. J. Control. Autom. Syst.*, vol. 17, no. 1, pp. 168–180, 2019, doi: 10.1007/s12555-017-0721-y.